



Published in final edited form as:

Neuroimage. 2012 September ; 62(3): 2065–2082. doi:10.1016/j.neuroimage.2012.05.065.

Ultra-High Resolution Diffusion Tensor Imaging of the Microscopic Pathways of the Medial Temporal Lobe

Michael M. Zeineh, M.D.-Ph.D.,
Stanford University

Samantha Holdsworth, Ph.D.,
Stanford University

Stefan Skare, Ph.D.,
Karolinska Institute

Scott W. Atlas, M.D., and
Stanford University

Roland Bammer, Ph.D
Stanford University

Abstract

Diseases involving the medial temporal lobes (MTL) such as Alzheimer's disease and mesial temporal sclerosis pose an ongoing diagnostic challenge because of the difficulty in identifying conclusive imaging features, particularly in pre-clinical states. Abnormal neuronal connectivity may be present in the circuitry of the MTL, but current techniques cannot reliably detect those abnormalities. Diffusion tensor imaging (DTI) has shown promise in defining putative abnormalities in connectivity, but DTI studies of the MTL performed to date have shown neither dramatic nor consistent differences across patient populations. Conventional DTI methodology provides an inadequate depiction of the complex microanatomy present in the medial temporal lobe because of a typically employed low isotropic resolution of 2.0–2.5mm, a low signal-to-noise ratio (SNR), and echo-planar imaging (EPI) geometric distortions that are exacerbated by the inhomogeneous magnetic environment at the skull base. In this study, we pushed the resolving power of DTI to near-mm isotropic voxel size to achieve a detailed depiction of mesial temporal microstructure at 3T. High image fidelity and SNR at this resolution are achieved through several mechanisms: (1) acquiring multiple repetitions of the minimum field of view required for hippocampal coverage to boost SNR; (2) utilizing a single-refocused diffusion preparation to enhance SNR further; (3) performing a phase correction to reduce Rician noise; (4) minimizing distortion and maintaining left-right distortion symmetry with axial-plane parallel imaging; and (5) retaining anatomical and quantitative accuracy through the use of motion correction coupled with

© 2012 Elsevier Inc. All rights reserved.

Correspondence Address: Michael M. Zeineh, Stanford University, 300 Pasteur Dr., Rm S-047, Stanford, CA, 94305-5105, t: 650-721-1419, f: 650-498-5374, mzeineh@stanford.edu.

Publisher's Disclaimer: This is a PDF file of an unedited manuscript that has been accepted for publication. As a service to our customers we are providing this early version of the manuscript. The manuscript will undergo copyediting, typesetting, and review of the resulting proof before it is published in its final citable form. Please note that during the production process errors may be discovered which could affect the content, and all legal disclaimers that apply to the journal pertain.

a higher-order eddy-current correction scheme. We combined this high-resolution methodology with a detailed segmentation of the MTL to identify tracks in all subjects that may represent the major pathways of the MTL, including the perforant pathway. Tractography performed on a subset of the data identified similar tracks, although they were lesser in number. This detailed analysis of MTL substructure may have applications to clinical populations.

Keywords

DTI; hippocampus; perforant pathway; tractography; medial temporal lobe; MRI

1. Introduction

The intricate circuitry of the medial temporal lobe (MTL) subserves mnemonic function in humans and non-human primates (Aggleton and Brown, 1999). Pathology of the MTL results in the memory complaints that form the hallmark of Alzheimer's disease (AD) (Giannakopoulos et al., 2009; Gómez-Isla et al., 1997; Mirra et al., 1991; Trojanowski and Lee, 2002). In particular, neurofibrillary pathology starts at the entorhinal cortex (ERC), the gateway of input and output between the hippocampus and the remainder of the neocortex (Braak and Braak, 1991). Cell loss in the ERC is marked in AD, particularly at early stages, and tangle-driven neurofibrillary pathology correlates well with memory complaints (Gómez-Isla et al., 1996; Hyman et al., 1984; Van Hoesen et al., 1991). This cell loss necessarily affects the perforant pathway, the main fiber tract connecting the ERC to the hippocampus proper (Suzuki and Amaral, 1994; Witter et al., 1989). Evaluation of the perforant pathway with diffusion tensor imaging (DTI) may provide insights into pre-clinical disease in the elderly, but identification of this tract has been elusive, with relatively few *in vivo* studies to date that only partially or indirectly image this pathway (Kalus et al., 2006; Yassa et al., 2010). Epilepsy often is clinically suspected to originate in the MTLs, but traditional methods of structural MRI often fail to identify an abnormality that is later proven surgically. Similar to AD, there have been only a few epilepsy DTI studies that have attempted to address medial temporal microstructure and micropathology (Salmenpera et al., 2006).

Isotropic high-resolution *in vivo* DTI studies of the MTL are absent in the literature. High-resolution acquisitions are needed to tease apart the anatomically distinct subregions of the MTL, but almost all *in vivo* DTI studies are done at 2.0–2.5mm isotropic resolution, including most studies done in AD and epilepsy (Zeineh et al., 2010). Of the few studies investigating the perforant pathway, one study utilized highly anisotropic voxel sizes to demonstrate changes in a fractional anisotropy (FA) based metric along the expected course of this pathway with aging (Yassa et al., 2010). Possibly because tractography algorithms require isotropic voxels to avoid significant bias (Jones and Leemans, 2011), Yassa et al. performed an anatomically based measurement rather than streamline-based tractography. An *ex vivo* study at 200 μm resolution of the hippocampus demonstrated stages of the perforant pathway, but required stopping points in tractography, possibly because of crossing-fibers (Augustinack et al., 2010).

In this study, we attempted to overcome a major obstacle of inadequate resolution and SNR by acquiring images at 1.4 mm isotropic resolution over several repetitions. Note, this is only 34%/17% of the voxel volume compared to a 2.0 mm/2.5 mm isotropic study, respectively, with a similar expected drop in signal-to-noise ratio (SNR). To achieve images with symmetric and minimal distortion, we have imaged in the axial plane using our in-house built generalized auto-calibrating partially parallel acquisition (GRAPPA) DTI sequence with a tailored reconstruction (Bammer, 2003; Griswold et al., 2002; S. Holdsworth et al., 2009; Qu et al., 2005; Skare et al., 2007). While eddy currents are typically addressed with twice-refocused preparations (Reese et al., 2003), this incurs a significant SNR penalty, which is prohibitive at this resolution. Instead, we performed an image-based higher-order eddy-current correction to align precisely the higher SNR single-refocused acquisition. Our final dataset was sinc-interpolated to 0.7mm isotropic voxel size.

To identify the tracts present in this high-resolution data set, all of our datasets were processed with deterministic tractography using the traditional (second-order) diffusion tensor model based on Gaussian diffusion because this is the most established and well-tested method in the literature (Basser et al., 1994). A significant problem in the field of tractography is that tracts are, at best, only synthetic representations of reality. At worst, they are fabrications and do not represent underlying structure. We visually compared tracts from all subjects with their expected trajectories. Additionally, we compared tractography results from subsets of each subject's data, i.e. only part of all the signal averages, to assess the sensitivity to noise as well as reproducibility of results with shorter acquisitions.

2. Methods

2.1 High-Resolution Diffusion Tensor Imaging

2.1.1. Acquisition—Six right-handed subjects provided written informed consent in accordance with Stanford's Institutional Review Board and Health Insurance Portability and Accountability Act compliance. Each subject was imaged on a GE 750HDx 3.0T magnet using an 8-channel receive head coil and body transmit (GE Healthcare, Waukesha, WI). A 2nd order high-order shim sequence achieved a uniformity of approximately 20Hz r.m.s. across the shimmed region of approximately 20 cm in size. Structural sequences included a localizer sequence and a direct coronal T₂-weighted FSE (TE 102 ms, TR ~7500 ms, 2mm skip 0, FOV 180–200mm, 384 × 256, flow compensation in the slice direction, ETL 15, bandwidth 64 kHz). In most subjects, a 3D sagittal T₂-weighted CUBE FSE (320 × 320, FOV 240, 1.2mm thick) and a 3D Ax T₁-weighted BRAVO SPGR (1mm isotropic) were also acquired at the end of the exam, as subject tolerance permitted.

The DTI acquisition was prescribed off the coronal T₂-weighted FSE and utilized the following parameters: axial plane echo-planar imaging (EPI), GRAPPA acceleration of 2 (Skare et al., 2007), number of signal acquisitions/shots 2, b-value 1500 s/mm², TR 3150 ms, TE 69 ms with a partial k-space acquisition (with 24 overscans, i.e. partial Fourier factor of 68.8%), single-refocused diffusion preparation, 70 diffusion-encoding directions, 10 b=0 mm/s² images, anterior-posterior phase-encode direction, chemical fat saturation, acquisition matrix 128 × 128, reconstruction matrix 256 × 256, 18cm FOV, slice thickness/gap = 1.4mm/0 mm, 27 slices, acquisition resolution of 1.4mm isotropic. Acquisition time was 8.5

minutes, and seven repetitions were performed in each subject. GRAPPA estimation and calibration were performed on all 10 $b=0$ images within each repetition (Skare et al., 2007), and the best GRAPPA weight set was applied to all other acquired volumes within each repetition (Samantha J Holdsworth et al., 2009). In order to benefit from complex averaging (i.e. reduced Rician noise), each individual DW image (each shot) was phase-corrected with the low-resolution image phase using a triangular-window (Pipe et al., 2002), modified for partial Fourier data, before averaging with the next shot. The disadvantage of complex averaging is that incomplete phase correction due to brain motion can result in destructive interferences in the final diffusion data (Skare et al., 2009). In this study, a triangular-window radius of 0.5 (percent of maximum k-space radius) was found to be an appropriate trade-off between reduced Rician noise and phase cancellations on complex-averaged diffusion data. The axial plane was utilized so that only single physical gradient coils were used for EPI readout and phase-encoding – this minimized ghosting artifacts due to anisotropic gradient delays (Reeder et al., 1999). Because the longitudinal extent of the hippocampus is oriented obliquely and the scans were acquired in the axial plane, the hippocampal tail fell outside the imaging field of view in most subjects. The reconstructed data was zero-filled in plane to achieve a voxel size of $0.7 \times 0.7 \times 1.4$ mm. The ten $b=0$ images were averaged into a single $b=0$ image for each repetition. The final isotropic voxel size of 0.7 mm occurs at the end of data pre-processing (See 2.1.2.E).

One subject had a hypointensity representing either an old small calcification or microhemorrhage in the high right frontal lobe. Since this subject had no neurologic complaints and reported that this lesion was known and remote, this data was included in this study.

2.1.2. Diffusion-Weighted Image Pre-processing (Figure 1, Online Supplementary Material Figure S1 and Table S1)

—Because we acquired the DTI data using a single-refocused diffusion preparation, images had higher SNR compared to twice-refocused preparations. The downside of single-refocusing is that each individual diffusion weighted image (DWI) has significant zero, first, and second-order eddy-current artifacts along the phase-encode (anterior-posterior) direction (Andersson and Skare, 2002; Haselgrove and Moore, 1996; Jezzard et al., 1998; Rohde et al., 2004; Xu, 2011). Without correction of these eddy-current artifacts, the combination of each DWI (each distorted in different patterns along the phase encode axis) would result in a final FA image that is blurred and inadequate for the determination of hippocampal microstructure. Here we developed and implemented a variant of the Rohde algorithm (Rohde et al., 2004) for correcting eddy currents. Our method uses slice-wise eddy-current correction to the 2nd order followed by 3-D motion correction. To preserve the ability to rotate the b-matrix, the repetitions were not averaged together. An example of axial and sagittal plane cine loops from one subject, before and after the correction procedure, is shown in Movie #1.

Each repetition (R) consisted of a single $b=0$ mm^2/s^2 image and 70 (D) directional diffusion-weighted images (annotated as $DWI_{R,D}$). For the purposes of the steps below, an isotropic diffusion weighted image ($isoDWIR$) refers to the average of all 70 DWIs within one repetition:

$$isoDWI_R = \frac{1}{70} \sum_{D=1}^{70} DWI_{R,D} \quad [1]$$

And the means of the individual DWIs across repetitions were computed as:

$$\overline{DWI}_D = \frac{1}{7} \sum_{R=1}^7 DWI_{R,D} \quad [2]$$

While isoDWIs computed on mean DWIs were calculated as:

$$\overline{isoDWI} = \frac{1}{70} \sum_{D=1}^{70} \overline{DWI}_D \quad [3]$$

The 5 steps in eddy-current and motion correction are as follows:

- A. Eddy-current correction (Figure 1 and S1, Table S1): An isoDWI was computed according to Eq. [1]. In a two iteration procedure, each slice was independently aligned with a 2nd order transformation field exclusively along the phase encode axis to this isoDWI. Eight harmonics are present in the 2nd order solution to the Laplace equation (B0/Z, X, Y, XY, YZ, XZ, X²-Y², 2Z²-(X²+Y²), see Table S1) (Rohde et al., 2004). Because an in-slice correction is used, two of the interaction terms (XZ and YZ) and the 2Z² term can be ignored because they reduce to linear terms in-slice (X, Y, and Z, respectively, see Table S1). This leaves the linear terms, the XY interaction term, and the X²-Y² and X²+Y² terms. It is a straightforward linear conversion of the X²-Y² and X²+Y² into the simpler X² and Y² terms (addition and subtraction, respectively), yielding six transformation parameters for each slice (Figure S1). A (Jacobian) brightness correction was employed to ensure that expanded voxels were darker than compressed voxels and vice-versa (Rohde et al., 2004). Most eddy-current correction methods use the b=0 image as a reference to which all DW images are aligned via mutual information registration. With the isoDWI used instead as a reference, a least-squares minimization was applicable since it has similar contrast to each DW image – an approach that is less complex and may be more suited to aligning low SNR DW images.
 - a. Iteration 1: For each slice, a modified version of the inter-correlation coefficient (ICC) algorithm offered an initial estimate of the X, Y, Z, and XY components (C₀-C₃) (Haselgrove and Moore, 1996). The algorithm, as published, measures the ICC between each phase-encode column of the source DWI image scaled at different magnifications with the same phase-encode column from the target b=0 image. The maximum of this matrix corresponds to the best shift and magnification for each phase encode column. Regressing the best shift across the phase-encode columns provides an estimate of the Z-component (shift – C₀) and X-component (shear – C₁)

as the intercept and slope of the regression, respectively. Similarly, the mean of the magnification across phase-encode columns approximates the Y-component (magnification – C_2). We made two modifications to this procedure: (1) The target is the isoDWI rather than the $b=0$ image, as it has similar contrast to the individual DWIs. (2) Rather than taking the mean of the magnification across the phase-encode columns, the magnification is regressed across phase encode columns. The intercept and slope correspond to the Y-component (magnification – C_2) and XY-component (trapezoidal distortion – C_3), respectively. These eddy-current components were estimated and images resliced with sinc interpolation using MATLAB (version 7.11.0; Mathworks, Natick, MA, USA).

- b. Iteration 2: After the first iteration, a slightly sharper version of the original isoDWI is created. The sum of squares of the difference between the transformed image and the new isoDWI across all six parameters was minimized using the `fminsearch` function in MATLAB, which uses a Nelder-Mead simplex algorithm.

This data processing took approximately 72 hours per subject on a 12-core power Macintosh (Apple, Cupertino, CA). As a final product of this step, one sinc-interpolation was performed on the raw reconstructed data.

- B. Motion Correction Across Repetitions: The relatively low-SNR DWIs were median filtered with a $5 \times 5 \times 5$ pixel kernel using `fslmaths` solely for calculation of alignment parameters to reduce the effect of noise on registration (Smith et al., 2004; Woolrich et al., 2009). The $b=0$ images and each median filtered DWI from the 2nd-7th repetitions were aligned to the corresponding image from the first acquisition using FSL's `flirt` (Jenkinson et al., 2002). We assumed that no motion occurs within a single DW volume acquisition (e.g. after a subset of slices had been acquired within a TR period); otherwise the volume would be corrupted.
- C. Motion Correction Across Diffusion Directions: The aligned 1st-7th repetitions were averaged across repetitions to make a composite series of \overline{DWI}_s using Eq. [2] and a composite $\overline{b=0}$ image using `fslmaths`. A composite \overline{isoDWI} was created by averaging across \overline{DWI}_s according to Eq. [3]. Each \overline{DWI} was then aligned using `flirt` to the \overline{isoDWI} .
- D. Motion Correction to $b=0$ Image: A final composite $\overline{\overline{isoDWI}}$ was again created by averaging this last set of aligned images. This $\overline{\overline{isoDWI}}$ was aligned to the composite $\overline{b=0}$ image using a correlation ratio cost function (the recommended inter-model function in FSL) and an affine transformation to compensate for any net eddy-current distortion in the $\overline{\overline{isoDWI}}$ and any relative motion between the $\overline{\overline{isoDWI}}$ and $\overline{b=0}$ image.
- E. Final Reslice: Alignments B-D were combined to a truncated sinc-interpolation with a Hanning window of 14 pixels using `flirt` and interpolating along the z-axis for 0.7mm isotropic reconstructed voxel size. As a final product of steps B-E, one additional sinc-interpolation was performed.

From the data originally reconstructed on the scanner, this combined eddy-current and motion compensation results in only two sinc-interpolation/resampling steps total (one for eddy-current correction step A, and one for motion correction steps B-D).

A mask was synthesized using FSL's brain extraction tool (BET) to zero-out the scalp and skull base (Smith, 2002). Additionally, any voxels that were zero for any diffusion-weighted component image in any repetition were included in the mask to ensure each voxel contained a full complement of data points. The rotation parameters were used to adjust the b-matrix for each repetition (Leemans and Jones, 2009). Thus, the repetitions were not averaged together.

One subject was uncomfortable after four repetitions of the diffusion sequence and needed repositioning. Because of differences in high-order shimming, the last three repetitions on this subject were not well aligned with the first four. Thus, the first four and last three repetitions were processed separately with steps A-C, and the last three repetitions were then aligned to the first four repetitions via an additional affine transformation of the respective \overline{isoDWI}_s as part of step D. Transformations were combined; therefore, no additional interpolation steps were required. An example of this subject's raw data sets and fully pre-processed data are also included in Movie # 2.

Images of the SNR was estimated using `fslmaths` and `fslstats` by measuring the mean signal and standard deviation over each pixel across the 10 serial b=0 images in each subject (Dietrich et al., 2007; Smith et al., 2004; Woolrich et al., 2009). The mean SNR was reported over all of the segmented MTL regions.

2.1.3. Diffusion Tensor Processing—With the software package Camino (Cook et al., 2006), images were processed with a 2nd order diffusion tensor model and nonlinear least squares tensor calculation (inversion model 2) to deliver images of fractional anisotropy (Alexander and Barker, 2005; Jones and Basser, 2004). Maps of tensor ellipsoids and fiber orientation were also generated using Camino's `sfplot` and `fslview`, respectively (Figure 4).

2.2 Subregional Analysis (Figure 2 and Figure 3)

The coregistered b=0 images, isoDWI, fractional anisotropy (FA), and mean diffusivity (MD) maps were visualized using ITK-SNAP (www.itksnap.org) (Yushkevich et al., 2006), which allows easy switching between imaging volumes. The coronal T2-weighted FSE, 3D T2-weighted FSE, and 3D T1-weighted BRAVO SPGR were viewed in an adjacent window using OsiriX (<http://www.osirix-viewer.com/index.html>) for a high-resolution reference. Segmentation of hippocampal subregions was performed manually according to anatomic atlases (Duvernoy, 2005; Insausti and Amaral, 2004; Yushkevich et al., 2009). Several approximations were made because of limitations in resolution and volume coverage. In keeping with the resolution of acquisition, all layers were a minimum of 2 pixels/1.4mm in thickness except where specified. Of note, the anatomy was best seen on the isotropic DWI (even better than on structural images), likely because diffusion weighting decreases the signal in white matter pathways and CSF, enhancing the overall contrast.

2.2.1. Full Segmentation Procedure—Three important anterior-posterior (A–P) landmarks were assessed in each hemisphere to assist in segmentation:

- A. The posterior boundary of the hippocampal head, best seen in the coronal plane, approximately marks the most posterior boundary of the entorhinal cortex (just posterior to Figure 3 Coronal Slab 4).
- B. The A-P location of the vertically oriented dark band of signal in the mid hippocampal head, here termed the vertical sheet of SRLMHS (stratum radiatum lacunosum moleculare and hippocampal sulcus), best seen in the sagittal plane (Figure 3 Sagittal section, at the A-P level of label #3). Segmentation of this region was necessary to separating CA 1 anteriorly (Slab 2) from CA3DG superiorly (Slab 3) and posteriorly (Slab 4), which is important for hippocampal head tractography. This procedure and the relevant anatomy are described in greater detail below.
- C. The A-P location where the posterior hippocampus begins bending medially, as seen in the coronal plane, marked the beginning of the hippocampal tail.

Much of the hippocampal tail and small portions of the posterior-most hippocampal body were not always included in the 27-slice volume depending on brain size and orientation. To control for variable amounts of hippocampal tail present, all segmentations were cut off at the posterior terminus of the hippocampal body.

The following regions of interest were segmented:

1. SRLMHS/HS (purple): Stratum radiatum lacunosum moleculare and hippocampal sulcus. This thin strip of dark signal seen in the central hippocampus likely represents myelinated axons (Benes, 1989) as well as cell layers from hippocampal field CA 1 (stratum radiatum, lacunosum, and moleculare) (Kerchner et al., 2010). Intermixed in this area are the remnants of the CSF-containing hippocampal sulcus. Additionally, partial voluming may occur with the molecular layer of the adjacent dentate gyrus, but for the sake of simplicity this is not considered further. The full anatomy of this strip is best depicted in cross-sectional atlases (<http://www.nitrc.org/projects/pennhippoatlas>) in the coronal and sagittal plane (Duvernoy, 2005; Yushkevich et al., 2009). In the hippocampal body and posterior hippocampal head, as seen in the coronal plane, this strip lies inferiorly and laterally to the central hippocampus (Figure 3 Slabs 4–6). In the mid-hippocampal head, as seen in the sagittal plane, this strip wraps around anteriorly and subtends at an approximately 40–60 degree angle to the long axis of the hippocampus (Figure 3, Sagittal section). Given the typical long axis of the hippocampus subtends about 20–40 degrees with respect to the horizontal axis in an *in vivo* experiment, this strip will be nearly 90 degrees (i.e. vertical) with respect to the horizontal axis, hence we term it the vertical sheet of SRLMHS. At our imaging resolution, segmentation of this vertical strip is an approximation: undulations in this strip are present (<http://www.nitrc.org/projects/pennhippoatlas>), the exact orientation of this strip varies by several degrees across the hippocampal head, and the superior part of the strip angulates posteriorly. All of these details are beyond the resolution of this study. Nevertheless, segmentation of this subregion, clearly evident in the sagittal image

in Figure 3, enables separation of the CA fields to allow for full hippocampal pathway analysis. Attention was paid slice-to-slice and in different orientations to ensure this region constituted a smooth, contiguous plane.

- a. For the hippocampal body and most of the hippocampal head, the coronal plane provided the best visualization. The SRLMHS extended medially to the opening of the hippocampal sulcus and laterally to the upper/outer corner of the hippocampus.
 - b. The vertical sheet of SRLMHS was best visible in the sagittal plane, and this helped colocalize in the coronal plane (Figure 3 Sagittal section and Coronal Slab 3). Generally this was visualized laterally, but it was sometimes difficult to visualize medially; in these cases, we approximated that the vertical sheet simply continued medially in the same coronal plane for the full width of the hippocampal head.
 - c. In the hippocampal head posterior to the vertical sheet of SRLMHS, the SRLMHS laterally overlies CA 1 and presumably contains CA 1 cellular layers (e.g. SRLM), but medially it overlies the subiculum and underlies CA3DG and does not contain CA 1 cellular layers (Slab 4). Therefore, this medial portion lacked SRLM and was labeled as a HS (hippocampal sulcus). In the hippocampal head anterior to the vertical SRLMHS sheet, this sub-classification was not necessary because the entire SRLMHS borders CA 1 superiorly and contains CA 1 cellular layers SRLM (Slab 2). This distinction is important because the SRLMHS will be a seed and target for tractography while the HS will not.
2. CA3DG (white): While cornu ammonis (CA) 3 and the dentate gyrus (DG) are separable with *ex vivo* imaging (Shepherd et al., 2007), they are not separable *in vivo*. Similarly, while others have segmented CA 2 as a separate subfield (Yushkevich et al., 2010), this is difficult to separate reliably with diffusion imaging, so CA 2 was incorporated into CA3DG.
 - a. In the hippocampal body, this was identified as all central hippocampal parenchyma. The lateral border included the hippocampal parenchyma extending directly superiorly from the SRLMHS in the coronal plane up to the superior boundary of the hippocampus as seen on the isoDWI. However, this subregion did not include the fornix or alveus as seen on the FA map.
 - b. In the hippocampal head, CA3DG was segmented posterior to the vertical sheet of SRLMHS, along the superior aspect of the SRLMHS, and including any of the gyrus uncinatus (the most medial posterior gyral component of the hippocampal head).
 3. CA 1 (dark brown):
 1. In the hippocampal body, this subregion was identified as a gray matter strip just lateral to CA3DG, sweeping in a curvilinear fashion inferiorly, with its

medial border just inferior to the most medial extent of the SRLMHS (Figure 3 Slabs 5 and 6).

2. In the posterior hippocampal head, posterior to and including the slice of the vertical sheet of the SRLMHS, the same border with CA3DG held laterally/superiorly, while the medial border of the inferior strip of tissue was at the same left-right location as the horizontal midportion of the hippocampal head (Figure 3 Slabs 3 and 4).
3. Anterior to the vertical SRLMHS sheet, the entirety of the hippocampal head was segmented as CA 1, including the first two slices of the gyrus uncinatus bordering the vertical sheet of the SRLMHS, with the exception of regions labeled as subiculum (Figure 3 Slab 2).
4. Subiculum (Subic, orange):
 - a. At the hippocampal body, this thin strip of tissue had a lateral border of CA 1. Its medial border was the most medial aspect of the parahippocampal gyrus, drawing an imaginary horizontal line medially from the midportion of the gyrus (Figure 3 Slabs 5 and 6).
 - b. In the hippocampal head posterior to the SRLMHS vertical sheet, the lateral border was identified as underlying the middle of the hippocampal head, adjoining the medial border of CA 1. This lateral boundary was maintained at the same left-right position throughout the entire hippocampal head. The medial border was at the medial upper corner of the parahippocampal gyrus throughout the entire hippocampal head (Figure 3 Slabs 2–4).
 - c. The gyrus uncinatus was labeled as subiculum from its superior border at the amygdalohippocampal area down inferiorly to the hippocampal sulcus, approximately two slices anterior to the vertical SRLMHS sheet (Figure 3 Slab 2 superomedially).
 - d. In the most anterior hippocampal head, where hippocampal interdigitations are not appreciable and where the SRLMS is no longer identified, all of the anterior hippocampus is subiculum (Figure 3 Slab 1). This portion was segmented in contiguity with the anterior-most gyrus uncinatus.
 - e. Due to resolution constraints, the presubiculum and parasubiculum were not segmented separately.
5. Entorhinal (ERC, red):
 - a. The most posterior boundary of the hippocampal head was considered the most posterior aspect of the ERC (just posterior to Figure 3 Coronal Slab 4). The anterior border was estimated 2mm (approximately 3 slices) posterior to the limen insula.
 - b. Throughout the hippocampal head, the ERC was defined as the cortex extending from the medial subicular border down to the fundus of the collateral sulcus. Anterior to the hippocampus at the level of the amygdala,

the ERC began at the sulcus semiannularis superiorly (best seen on the coronal T2 FSE images) and extended inferiorly to the fundus of the collateral sulcus. The gyrus ambiens and intrarhinal sulcus were considered part of the ERC.

- c. The lateral boundary was shifted according to the depth of the collateral sulcus (Insausti et al., 1998). If the collateral sulcus was interrupted when panning through coronal slices, this lateral entorhinal border was kept at a similar position compared to slices where the collateral sulcus was present. If two collateral sulci were present, the more medial sulcus was used.
6. Perirhinal (PRC, dark blue):
 - a. This was defined as all cortex lining the collateral sulcus on the same slices that ERC is present, just lateral to the entorhinal cortex (i.e. only anteriorly at the level of the hippocampal head, Figure 3 Slabs 1–4).
 - b. A very thin strip of perirhinal cortex does extend posterior to the entorhinal cortex (Insausti et al., 1998), but this was judged as too difficult to segment accurately.
 - c. PRC was defined as extending six sections anterior to the anterior ERC border (4.2mm). At the level of the limen insula, the dorsomedial border was the most medial point of the parahippocampal gyrus. More anteriorly, the dorsomedial border was the fundus of the temporopolar sulcus. If the collateral sulcus was present, its lateral border formed the ventrolateral border of the PRC. If it was interrupted, the location of an adjacent slice containing the collateral sulcus was used.
 7. Parahippocampal Cortex (PHC, yellow):
 - a. All of the cortex along the medial bank of the collateral sulcus and extending adjacent to the subiculum, posterior to the PRC, extending posterior to the level of the posterior-most hippocampal body (Figure 3 Slabs 5 and 6).
 8. Cingulum (bright green):
 - a. Single slices designating the anterior and posterior parahippocampal gyral white matter were selected and all of the parahippocampal gyral white matter was segmented. The lateral boundary chosen was an imaginary line between the fundus of the collateral sulcus and the infero-lateral corner of CA 1. If the collateral sulcus was interrupted and not present on the selected slice, it was estimated as being at a similar position on the closest available slice. The two locations in the coronal plane were:
 - i. Anteriorly at the level of the vertical SRLMHS sheet (Figure 3 Slab 3).
 - ii. Posteriorly at the level of the posterior-most hippocampal body.
 9. Alveus and Fornix (dark green): Both of these are best seen on the FA maps and T2-FSE images. Because there is partial voluming with adjacent white matter

superiorly, we ensured that these subregions did not extend above the level of the temporal horn as seen on the isoDWI sequence.

- a. The posterior fornix was segmented at the posterior-most two coronal slices where it was completely visualized (its more posterior portion was sometimes cut off more superiorly). The medial forniceal border extended to but not beyond the medial border of CA3DG. Partially visualized portions remaining posteriorly were included in the posterior fornix.
- b. The alveus is a very thin strip of white matter on the top of the hippocampus that feeds into the fimbria of the fornix, faintly seen on the T2 FSE images and more clearly seen on the FA maps. The alveus and fimbria of the fornix were labeled as a combined region called the alveus, and segmented together throughout the entire extent of the CA 3 field as well as overlying the hippocampal head. This was brought in contiguity with the superior aspect of CA 1 and CA 3. Because of partial voluming with other subregions, on some slices this layer was 1-pixel thick or not visible.

The entire segmentation procedure takes approximately ten hours per subject. A similar method of segmentation (Zeineh et al., 2003) resulted in a high intra-rater reliability (Burggren et al., 2008). In our subject pool, most of the anterior mesial temporal structures were imaged in their entirety with the exception of inferior portions of the ERC and PRC in some subjects. For these anterior structures, in regions where the ERC and PRC were simply one slice below the cutoff as visualized on the $b=0$ image from the first repetition, the ERC and PRC were approximated as the adjacent subcortical white matter. If these cortical regions were more than one slice below the cutoff, they were not segmented.

2.2.2. Subregion statistics (Table 1)—Median FA, and median MD were computed within each segmented subregion using `fslstats`. Subregion SRLMHS was combined with CA3DG because SRLMHS was considered to be too small to reliably analyze on its own. Similarly, the fornix was combined with the alveus. The median was used rather than the mean to compensate for partial voluming with the adjacent CSF spaces and parahippocampal gyral white matter, which both have significantly different FA and MD than gray matter, as a very rough way of approximating mid-cortical measurements. Subregional volumes were not analyzed because EPI images with distortion and inferior resolution (compared to SPGR T1 images) are not suitable for cortical volume calculations. With each ROI in each subject constituting a separate observation, left and right sides were compared using a paired t-test for all observations ($n=6$ subjects \times 7 ROIs = 42) using the `ttest` function in Excel (Microsoft Corp., Redmond, WA, USA). For individual ROIs, a paired t-test was also performed ($n=6$). P-values were not corrected for multiple comparisons.

2.3 Tractography

2.3.1. Tractography – Parameter Validation (Table 2, Figure 5)—Our goal was to find the optimal tractography parameters that demonstrated tracts of interest in the native raw data, but which reduced tracks (and thus reduced false positives) in the presence of noisier data. Thus, we compared tractography on the seven-repetition dataset with just

processing the noisier first repetition on its own. We performed bidirectional streamline tractography with Camino using the default Euler method (Basser et al., 2000) and tensor interpolation at a step size of 0.07 mm (1/10th of the voxel size) between the ERC and fields CA3DG and CA 1/SRLMHS (pathway #2 below) while varying the:

- Minimum track length, which discards tracks shorter than a certain length
 - 10 and 20 mm (we did not include 0mm, the default in Camino, because it would result in too many false positives given that many of the ROIs are adjacent to one another).
- Curvature threshold, which stops tractography if the tract curvature exceeds the angular threshold
 - 20 – 90 degrees in increments of 10 (the default in Camino is 80 degrees)
- FA threshold, which stops tractography if the current voxel has a lower FA than the threshold
 - 0.02, 0.05, and 0.1 (the default in Camino is 0)

2.3.2. Tractography - Application—Connectivity of the medial temporal lobe has largely been established through animal tracing studies, and the pathways below depict the major connections (Insausti and Amaral, 2004). We searched for the following tracks bidirectionally (i.e., each region served as both a seed and a target, and fibers were summed):

1. *Cingulum*: (Figure 2-1 – Orange, through plane). This bundle of white matter progresses antero-posteriorly throughout the parahippocampal gyrus containing numerous white matter tracks -- in particular the cingulum bundle which contains fibers from the cingulate gyrus and frontal lobe (See Figure 6.1 from (Goldman-Rakic et al., 1984; Mufson and Pandya, 1984)). Although we did not image the cingulate gyrus or the frontal lobe for this study, given the importance of this pathway and preponderance of these fibers in the parahippocampal gyrus, we have included it in our analysis.
 - a. Seeded/targeted the anterior cingulum.
 - b. Seeded/targeted the posterior cingulum.
2. *Perforant*: (Figure 2-2 - Yellow). The perforant (internal) and alvear (external) pathways project from the ERC to the hippocampus Entorhinal neurons would be expected to penetrate the subiculum en route to the dentate gyrus and hippocampal CA fields (perforant) or extend along the infero-lateral surface of the hippocampus to synapse on the CA fields (alvear path) (See Figure 8 from (Hevner and Kinney, 1996; Mufson et al., 1990)).
 - a. Seeded/targeted the ERC.
 - b. Seeded/targeted fields CA3DG, CA 1, and SRLMHS.
 - i. These fibers can cross or terminate in the SRLMHS.

3. *Fornix*: (Figure 2-3 – Dark Blue). This track largely originates in CA 3 and the subiculum, and extends in the alveus and fimbria of the fornix to the fornix (Figure 12.4 from (Nieuwenhuys et al., 2008)). The cruz (posterior pillar) of the fornix was not within the field of view of this experiment.
 - a. Seeded/targeted CA3DG and the subiculum, the major sources of input to the pre-commissural and post-commissural fornix, respectively (Swanson and Cowan, 1975, 1977).
 - b. Seeded/targeted the posterior fornix.
4. *Schaffer Collaterals*: CA3DG to CA 1/SRLMHS (Figure 2-4 – Pink). CA 3 neurons send output to the fornix and have collateral processes that extend along both the inner and outer surface of CA 1 to synapse on stratum radiatum, stratum oriens, and the pyramidal cell layer of CA 1. This would include potential endofolial fibers (Lim, Mufson, et al., 1997). While some projections go via an inferior approach to the basal dendrites of CA 1 in the stratum oriens, others go via a superior approach to the stratum radiatum of CA 1 (Swanson et al., 1978), so SRLMHS was included as a target region (See Figure 12.8 from (Nieuwenhuys et al., 2008)).
 - a. Seeded/targeted CA3DG.
 - b. Seeded/targeted CA1 and the SRLMHS.
5. *CA 1 to Subiculum* (Figure 2-5 – Green). The output from CA 1 extends inferiorly and curves towards the subiculum (Amaral et al., 1991; O'Mara, 2005), so SRLMS was not included as a seed/target.
 - a. Seeded/targeted CA 1.
 - b. Seeded/targeted the subiculum.
6. *Subiculum to ERC* (Figure 2-6 – Purple). This primary output of the subicular complex (including the presubiculum and parasubiculum) is a direct connection to the entorhinal cortex to complete the hippocampal circuit loop (Köhler, 1984). While the subiculum has widespread connections throughout the brain (Rosene and Van Hoesen, 1977), these are beyond the scope of this work because of the limited field of view in this study.
 - a. Seeded/targeted the subiculum.
 - b. Seeded/targeted the ERC.
7. *ERC to perirhinal/parahippocampal cortices* (Figure 2-7 – Light Blue). The ERC has both direct projections to and from these adjacent cortical areas (Suzuki and Amaral, 1994; Van Hoesen and Pandya, 1975)
 - a. Seeded/targeted the ERC.
 - b. Seeded/targeted the combined PRC/PHC.

The Camino function track generates streamlines starting at a seed point using the Euler method (Basser et al., 2000). We chose tensor interpolation at a step size of 0.07mm, and tracks were stopped if the curvature surpassed a conservative threshold of 40 degrees or the FA dropped below a threshold of 0.05 as (both thresholds per the results of the parameter optimization).

The Camino function `procstreamlines` then allows for truncation or removal of streamlines. Streamlines were truncated when they entered a target region. However, streamlines were not truncated within the seed region (this is the default behavior of the program). While this does result in streamlines traversing the seed ROIs, it is appropriate to keep the seeding voxel to depict the origin of the generated streamline. After truncation, streamlines were kept only if they connected the seed and target regions of interest and met the minimum tract length criteria of 10mm (this threshold was again chosen from the parameter optimization).

Total fiber counts as well as their mean and standard deviation were tabulated separately for each hemisphere as well as the ratio of left to right sided fibers (Table 3). The left and right sides were compared with a two-sided paired t-test. To normalize for differences in the number of fibers in the pathways, we also compared the left-to-right ratio also using a t-test, with the null hypothesis of a ratio of 1:1.

The FA, mean diffusivity (MD), and tract length were averaged along the path of each track in each subject using Camino's `tractstats` function (Table 4), and compared between the left and right sides with a paired t-test.

Meshes from the segmentation were created using ITK-SNAP, and fiber tracks were superimposed on these meshes and the isoDWI using Paraview (www.paraview.org) with a line width of 2 to generate tractography figures. All images are depicted in radiologic format.

2.4. Analysis of Data Subsets

To see if the above results can be replicated with shorter imaging acquisitions, one to six subsets of the repetitions were analyzed. More specifically, subset 1 denoted the 1st repetition, subset 2 denoted the 1st through 2nd repetitions, and subset N denoted the 1st through Nth repetitions. Additionally, we analyzed the last three subsets to compare to the first three subsets.

- Subregional FA and MD were computed for each subset in the same manner as for the 7-repetition dataset.
- Fiber counts (Table 5) and tract based FA, MD, and length were similarly calculated and analyzed for each subset.
- To further analyze the tracts of the subsets, we computed the Dice coefficient (Dauguet et al., 2007) between each subset and the seven repetition dataset (Table 6). The Dice coefficient was calculated by first converting each set of tracks to a volumetric image at a voxel size of 0.7mm isotropic. This step binned the tracks into the nearest voxel using the `procstreamlines` function with the `output_acm` option. We call this image R_S , with S denoting the subset. The coefficient was then

calculated using the following formula (Dice, 1945) using `fslmaths` and `fslstats`:

$$D(R_s, R_7) = \frac{2 * \text{card}(R_s | R_7)}{(\text{card}(R_s) + \text{card}(R_7))} \quad [4]$$

3. Results

3.1 High-Resolution Diffusion Tensor Imaging (Figure 3 and Figure 4)

The mean SNR across subjects on the $b=0$ images was 10.96 ± 1.26 . The expected SNR across the seven repetitions would be approximately 28.98 (this was not directly calculated because the repetitions were not averaged to preserve the ability to correct the b-matrix for motion; instead we multiplied by the square root of seven). The image processing methods fully corrected for eddy current-induced image warping and subject bulk motion (Movies #1 and #2). Diffusion tensor processing produced detailed maps of hippocampal and adjacent cortical microstructure: the images of fractional anisotropy display not only cortical FA within the 6-layer entorhinal cortex but also intrahippocampal FA within the 3-layer hippocampal allocortex (Figure 3 and Figure 4). Superimposing the principal directions demonstrates the orientation of the cingulum bundle within the parahippocampal gyrus, intra-hippocampal orientation, and the suggestion of perforant path fibers directed towards the hippocampus (Figure 4).

3.2 Subregional Analysis (Table 1)

Comparing the left and right side across all MTL subregions and subjects ($n=6$ subjects \times 7 subregions = 42), FA was higher on the left side and MD was lower on the left side (p -values of 0.026 and 0.001, respectively). Examining each subregion separately, FA was higher in the left ERC ($p=0.014$) while MD was lower in the left alveus/fornix ($p=0.006$).

3.3 Tractography

3.3.1. Parameter Validation (Table 2, Figure 5)—We quantified tractography from ERC to CA3DG, CA 1, SRLMHS (pathway #2) with the goal of optimizing the number of presumed real fibers obtained from the full set of data (seven repetitions of the diffusion acquisition scheme) while still demonstrating noise sensitivity (fewer fibers on the one repetition data set). We evaluated tracts while varying the FA threshold, curvature threshold, and minimum tract length and found that:

- Data were sensitive to noise at FA thresholds of 0.02 (under all curvature criteria), 0.05 (with a curvature criteria of 60 degrees or less), and 0.1 (curvature 30 degrees or less). An explanation for this finding is that the intrahippocampal FA can dip below 0.1, causing tractography to miss perforant path fibers with a higher FA threshold, increasing presumed false negatives. Conversely, while more fibers are present with a FA threshold of 0.02, the top row of Figure 5 demonstrates a spurious fiber on both sides crossing the tentorium (white arrows), clearly a false positive crossing into the CSF. Consequently, a threshold of FA of 0.05 was a reasonable trade-off between more fibers and fewer false positives.

- The lower the curvature, the greater the noise sensitivity, at a cost of fewer fibers overall. A threshold of 40 degrees also seemed to be a reasonable balance between noise and number of fibers.
- Finally, with regard to minimum track length, more tracks were present at the minimum track length of 10 mm, which is preferable for some of the relatively short pathways between neighboring structures. As an example, the middle row of Figure 5 shows a small, presumed left perforant path tract identified only on the shorter threshold (blue arrows).

These thresholds are more conservative than those established by specimen tractography (Dauguet et al., 2007; Dyrby et al., 2007)

3.3.2. Tractography – Application (Figure 6-1 to 6-7, Movies #3-1 to #3-7, Table 3 and Table 4)

1. *Cingulum*: The cingulum bundle extended in a symmetric fashion throughout both parahippocampal gyri. Some of the termini of the tracks appear slightly outside the boundaries of the seed/target ROIs, but this is secondary to approximations made in the 3D rendering of the ROIs.
2. *Perforant*: Several fiber bundles were present between the ERC with CA3DG, CA 1, and SRLMHS bilaterally in all subjects, with the greatest concentration near the hippocampal head, which may represent the angular bundle. Many fibers followed the alvear path extending around the hippocampal body and head, while some project through the subiculum (light brown, not a target or seed in this pathway) en route to the hippocampus. While medial entorhinal fibers connected to both the anterior and posterior hippocampus, the few lateral entorhinal fibers largely connected to the posterior hippocampal body (subjects 2, 4 and 6 bilaterally).
3. *Fornix*: Fibers between the fornix and CA3/subiculum took the expected route circumferentially around the hippocampus, coursing in the alveus, which lies immediately superior to CA 3. The majority of fibers involved the hippocampal head and subiculum. Some fibers arced outward from the hippocampal head (subject 6 on the right), possibly a false positive.
4. *Schaffer Collaterals*: Many fibers take the expected path along the outer surface of CA 3 and CA 1 (within the alveus), while fewer course along the inner surface (behind CA 1 in brown). Most, but not all, of the fibers are closely adherent to the hippocampus as expected.
5. *CA 1 to Subiculum*: Many fibers took the expected course along the undersurface of CA 1 and the subiculum. Some took a direct path within a similar coronal section, whereas other fibers connected more disparate parts of the two fields. Again, some fibers were not as close to the hippocampal head or body as expected.
6. *Subiculum to ERC*: Connections were seen between the ERC and the anterior as well as posterior subiculum. Because perforant pathway fibers are expected to cross the subiculum en route to the hippocampal CA fields, there is necessarily some

overlap between ERC-Subicular tracts and perforant pathway tracts. Nevertheless, many ERC-subicular tracts are unique and not apparent in pathway #2 above.

7. *ERC to perirhinal/parahippocampal cortices*: Subcortical U-fibers constitute the tracts between the ERC and PRC, while longer-range fibers extend between the ERC and PHC.

A paired comparison of the overall numbers of tracts on the left and right sides across all pathways was not significant ($p=0.62$). However, the ratio of left to right sided tract counts across all pathways in all subjects was slightly higher on the left side (ratio of 1.27 ± 0.87 , $p=0.05$, $n=7$ pathways times 6 subjects = 42). No individual pathway showed significant lateralization as measured by this ratio.

Tract-based measurements of FA, MD, and tract length (Table 4) across all pathways and subjects demonstrated no left-right symmetry for FA ($p=0.083$), a lower MD on the left ($p=0.042$), and longer tracts ($p=0.019$) on the left side. Examining individual pathways across subjects demonstrated no significant left-right differences.

3.4. Analysis of Data Subsets

- Higher FA and lower MD across the full set of subregions as well as higher ERC FA and lower forniceal MD remained significant ($p<0.05$) for all of the data subsets.
- The major pathways were intact with fewer repetitions of the diffusion scheme, albeit with lower track counts (Table 5). The asymmetric ratio of left-sided to right-sided fiber counts did not reach significance with the data subsets, though for some of the subsets the ratio did approach significance. Directly comparing total tract counts from the 1st-6th subsets with the superset of the 7-repetition data set showed that all other subsets were significantly different ($p<0.04$ for all other subsets). Comparing all pathways from the first 3-repetition subset with the last 3-repetition subset revealed very similar fiber counts from independent diffusion-weighted data sets ($n=84$, $p=0.486$).
- Tract-based FA was significantly higher on the left for data subsets 6, 5, 4, 3, and 2, but not for the 7, 1, or last 3-repetition subsets. An explanation for the lack of significance with the full data set and last 3-repetition subset may be that there is more incompletely compensated motion at the last repetition confounding any analysis that included this last repetition. Similarly, the first subset would be expected to be noisy in isolation. Tract-based MD was lower on the left only for the 7, 6 and 3-repetition datasets. Finally, tract length was greater on the left only for the 7, 6, 3, and 2-repetition data sets.
- The Dice coefficient analysis showed that larger white matter bundles such as the cingulum were fairly consistent across subsets, whereas the perforant pathway was much less consistent as the number of subsets was reduced (Table 6). Similarly, this more sensitive comparison shows that the first 3-repetition and last 3-repetition subsets had considerably less overlap than might be expected from their rather similar fiber counts.

4. Discussion

This is the first *in vivo* or *ex vivo* DTI study in humans to demonstrate a contiguous depiction of the perforant pathway in all examined human subjects, as well as to visualize the entire extent of each stage of intrahippocampal and parahippocampal circuitry. It was essential to acquire data at a high isotropic resolution of 1.4mm and perform image processing to correct for motion and eddy currents while retaining SNR. This important advance may permit interrogation of clinical alterations in MTL circuitry at a level of detail that has not been possible.

Previous attempts have not achieved this goal primarily because of inadequate resolution, and instead these studies have focused on the parahippocampal gyral white matter. One study on the perforant pathway in the elderly utilized markedly anisotropic voxels ($0.66 \times 0.66 \times 4\text{mm}$), so rather than performing streamline tractography, the perforant pathway was estimated based on anatomy (Yassa et al., 2010). A composite metric assessed to what extent tensor ellipsoids followed this estimated pathway, resulting in differences between younger and older individuals. Another study in normal volunteers utilized probabilistic tractography with approximately 2mm isotropic voxels to identify tracks throughout the parahippocampal gyrus, and they found 3/10 volunteers exhibited parahippocampal-hippocampal connectivity (Powell et al., 2004). In our current study, we found 6/6 subjects with such tracks present bilaterally. One study in AD used intervoxel coherence of the parahippocampal gyrus as a surrogate for the perforant pathway utilizing approximately 2.5mm isotropic voxels; here they identified differences between AD and normal controls in the hippocampus, entorhinal cortex, and perforant pathway zones (Kalus et al., 2006). Finally, an *ex vivo* 0.2 mm study on hippocampal specimens demonstrated portions of the perforant pathway that were corroborated by histology (Augustinack et al., 2010). In this study, they required two steps to track the full extent of the perforant pathway, with a stopping point in the subiculum. One reason that tracks terminated in the subiculum may be that DTI-based streamline tractography could not propagate through a region of crossing fibers. However, our work also utilized DTI-based tractography, and we do find continuous perforant pathway tracks in all subjects. Another contributing difference between our studies is that the histologic DTI necessarily utilizes a small field of view, while our *in vivo* work has a larger field-of-view. This larger field-of-view may capture contiguous perforant pathway fibers (e.g. from the ERC anterior to the hippocampal head as seen in Figure 6-2) that are not subject to as severe a crossing-fiber challenge.

A significant challenge to DTI of the hippocampal pathways is the lack of a gold standard for these projections in humans. One *ex vivo* study of human specimens utilized the diffusible lipophilic tracer DiI to identify connections with the fetal entorhinal cortex; this suggested that the alvear pathway is an important component in addition to the perforant pathway (Hevner and Kinney, 1996). In our study, we also see both presumed perforant and alvear pathway fibers. Additionally, pathway number four in our study follows the expected trajectories of not only the Schaffer collateral pathway, but also the endofolial pathway, which was also uniquely identified in humans using *ex vivo* tracing methods (Lim, Mufson, et al., 1997). However, mossy fibers are far beyond the resolution of this study (Lim, Blume, et al., 1997).

The number of perforant pathway fibers is lower than expected when compared to other stages of the circuitry; considering the entire area of the ERC, there are fewer fibers emanating from the structure compared to other stages of the circuitry and many fewer than may be expected. This may be due to the known challenge of crossing fibers because perforant pathway axons penetrate the subiculum en route to the hippocampus. Along these lines, pathway depictions in this study primarily involve the anterior hippocampus, possibly because these elements of the circuitry involve the least number of fiber crossings. Another source of uncertainty is the observation that the subiculum and CA 1, like the remainder of the neocortex, both demonstrate a significant fractional anisotropy and orientation, best seen *ex vivo* (Ozarlan et al., 2009; Shepherd et al., 2007). We see this anisotropy in our imaging data (Figure 3, Figure 4B and D), further evidence of the fine detail evident in this study. It is unclear if this cortical anisotropy reflects cellular and/or axonal orientation, and tractography is hence limited by this uncertainty. Future studies utilizing tractography that can resolve crossing fibers may prove beneficial for both *in vivo* and *ex vivo* studies. Finally, in this study we were unable to image fully the hippocampal tail because of limitations on the number of slices that can be acquired in the axial plane with our desired high SNR. While we do see a suggestion of the expected connections between the lateral entorhinal cortex and the posterior hippocampal body (Witter et al., 1989), future work imaging the whole hippocampus may allow for a more detailed interrogation of this pathway.

In this experiment, a region of interest analysis showed that FA was higher and MD lower on the left side. Our FA and MD values are similar to those reported in the literature, though our MD measurements are at the lower end (Müller et al., 2006). This difference may be due to less partial voluming with CSF in our work because of the higher resolution. Similarly, tract-based MD was lower and the tract length was longer on the left side. Finally, while a group level comparison of fiber counts did not demonstrate more tracks on the left compared to the right side, assessing the ratio of left to right proved to be significant. The ratio may be more sensitive because it controls for variations in the baseline number of fibers between pathways. At the same time, the ratio may be very susceptible to noise; the 1-repetition subset analysis had a p-value unexpectedly close to the 7-repetition analysis. Similarly, the tract-based measures were present inconsistently when analyzing data subsets, implying a similarly high variance in these measures. Nevertheless, all of these findings may reflect a property of the tensor ellipsoids: they may be more coherent and/or strongly oriented along the steps of MTL circuitry in a lateralized manner across a group of subjects. Considering that this study examined right-handed cohort of normal volunteers, this suggests a correlation with language lateralization. This left-right asymmetry has been observed for FA as a similarly small effect in the hippocampus, though MD did not follow in the same direction (Müller et al., 2006). Similar entorhinal left-right differences in MD have also previously been reported (Rose et al., 2006). Forniceal differences have not been clearly identified in normals (Malykhin et al., 2008), though in our study we only had limited visualization of the fornix. The asymmetry we observe in this study is mild and only at a group level. Nevertheless, there remains a chance that lateralizing abnormalities in groups of patients will be apparent with this technique, though the sample size of our study is admittedly small.

This work involves an extremely detailed segmentation of the medial temporal lobe. The diffusion-weighted images displayed sufficient isotropic resolution and contrast to discern hippocampal substructure. This enabled us to fully segment the subfields of the hippocampal head and body, a feat previously accomplished only *ex vivo* (Yushkevich et al., 2009) and in one other *in vivo* study (Van Leemput et al., 2009). The segmentation was performed on the diffusion-weighted images themselves, so there are no issues of misalignment that can take place if segmentation is performed on structural images. For the same reason, however, this segmentation is not volumetric because distortions still exist in EPI data. Some limitations do exist in our ability to segment. In particular, CA 2 is difficult to define on serial sections in anatomic atlases, so it was approximated as part of CA 3. The dentate gyrus projections to CA 3 are a target we did not assess because of the difficulty in discriminating the dentate gyrus from CA 3 with *in vivo* imaging.

For any method of tractography, it is critical to have high quality diffusion-weighted data, but DTI utilizing EPI is plagued by many sources of artifacts, which is further complicated by the fact that methods of artifact reduction often reduce SNR. Eddy-current artifacts can obfuscate tractography, so we have employed a variant of an established eddy-current correction algorithm (Rohde et al., 2004) to achieve a precise image registration. Our algorithm registers to the isoDWI, which facilitates alignment between images with similar contrast. Additionally, we separate eddy-current correction from motion correction so that fewer variables are optimized simultaneously. However, our method is suitable only for minimal motion between acquisitions because motion can disrupt the eddy-current correction process and vice-versa. Our future work will include a more formal unification of both methods of eddy-current correction that will have more general applicability. Apart from eddy currents, echo-planar distortion can obscure visualization of the temporal lobes, and secondary distortion can be left-right asymmetric because of variable pneumatization of the petrous apices. Some work has pursued coronal plane imaging with a small field of view to minimize distortions, though it becomes challenging to have contiguous slices with this approach and consecutive interleaves are required (Salmenpera et al., 2006). In our work, we have chosen to preserve SNR, minimize ghosting, and keep distortion left-right symmetric by using conventional axial-plane imaging with the phase-encode axis anterior-posterior. We employ complex averaging to minimize the impact of Rician noise that can contaminate images with low underlying SNR, but limit the impact of phase cancellations with an appropriate threshold for complex averaging. We accelerate by a factor of two in this study, and the g-factor related SNR loss is ameliorated by the significant shortening of the TE. Further parallel acceleration would reduce distortions and further improve asymmetry, but the TE benefit would be minimal, and SNR and the ability to image at high spatial resolution would be compromised. Our future work will incorporate methods to correct EPI distortions that are still present with parallel imaging (Embleton et al., 2010). This will facilitate a direct registration of structural images with DTI, enabling easier or even semi-automatic segmentation of the MTL (Yushkevich et al., 2010).

To evaluate the sensitivity of this method to noise, we analyzed subsets of the data, which showed an expected reduction in fiber counts. This suggests that these tracks arise from something other than noise. One could speculate that the tract parameters we measure are

reflective of tissue connectivity; however, without a gold standard, this claim is difficult to substantiate. While the tracks appear to reflect the known anatomy, caution in interpretation is still appropriate. For example, tracks 3, 4, and 5 all demonstrate some fibers arcing too far forward anteriorly, which are likely to be false-positives. This could be ameliorated by imposing more tractography constraints including exclusion zones and waypoints. However, for the purpose of this study we sought to minimize the ROIs to enable the tracking algorithms to be guided by the tensor field, not anatomic constraints. While some false-positives are evident, this depiction does provide a better sense of the noise in generating the pathways. This limitation with false-positives exists for any streamline approach because tractography has yet to be conclusively proven. Other approaches include bootstrap techniques that account for noise across multiple repetitions and compute confidence measures of connectivity (Jones, 2003). Probabilistic tractography employs thousands of iterations coupled with randomization in a Monte-Carlo approach to estimate the probability of connectivity (Parker et al., 2003). These analysis methods may have benefits in quantifying differences between normal and diseased states, and our future work will investigate their applicability.

Clinical protocols need to be efficient for practicality, and one hour of diffusion imaging may not be feasible. However, the SNR for three or four repetitions of this study would be approximately 19 and 22, respectively, keeping in line with the minimum requirements for SNR in DTI studies (Jones and Leemans, 2011). Subtle left-right difference in tractography parameters, however, is not consistently observed with less than the full set of repetitions of our data set. Similarly, for the perforant pathway, the Dice coefficients dropped substantially when using three repetitions. The number of repetitions needed may depend on the suspected differences in FA, MD, or other track parameters for the clinical question.

Conclusion

In this study, we have used advanced diffusion MRI acquisition and data processing techniques to create detailed maps of medial temporal lobe architecture. Tractography demonstrates pathways that closely parallel connectivity known to be present in animal studies. There is promise for this methodology in clinical applications involving mesial temporal pathology, particularly in clinical scenarios where disruption of pathways due to cell loss is suspected. Detecting such abnormalities may improve clinical diagnoses and facilitate the development of interventions.

Supplementary Material

Refer to Web version on PubMed Central for supplementary material.

Acknowledgments

This work was supported by an RSNA Research Fellow Grant. We would like to acknowledge GE Healthcare for their support, R. Scott Hinks and Dan Xu for their discussion regarding eddy currents, Anh Van for her support with image reconstruction, David Rex for his conversations on image acquisition and processing, and Geoffrey Kerchner for his comments on this manuscript.

Sources of Support: RSNA Research and Education Foundation Research Fellow Award General Electric

Abbreviations used

MTL	Medial Temporal Lobe
AD	Alzheimer's Disease
DWI	Diffusion Weighted Image
DTI	Diffusion Tensor Imaging
EPI	Echo-Planar Imaging
FA	Fractional Anisotropy
MD	Mean Diffusivity
isoDWI	isotropic diffusion weighted image, b=0 Image: $b = 0 \text{ s/mm}^2$ (no diffusion weighting) image
GRAPPA	Generalized Auto-calibrating Partially Parallel Acquisition
ERC	Entorhinal Cortex
PRC	Perirhinal Cortex
PHC	Parahippocampal Cortex
CA	Cornu Ammonis
DG	Dentate Gyrus
CA3DG	Cornu Ammonis 3 and Dentate Gyrus
Subic	Subiculum
SRLMHS	Stratum Radiatum Lacunosum Moleculare and Hippocampal Sulcus
HS	Hippocampal Sulcus

References

- Aggleton JP, Brown MW. Episodic memory, amnesia, and the hippocampal-anterior thalamic axis. *Behav Brain Sci.* 1999; 22:425–444. discussion 444–489. [PubMed: 11301518]
- Alexander DC, Barker GJ. Optimal imaging parameters for fiber-orientation estimation in diffusion MRI. *Neuroimage.* 2005; 27:357–367. [PubMed: 15921931]
- Amaral DG, Dolorfo C, Alvarez-Royo P. Organization of CA1 projections to the subiculum: a PHA-L analysis in the rat. *Hippocampus.* 1991; 1:415–435. [PubMed: 1727001]
- Andersson JLR, Skare S. A model-based method for retrospective correction of geometric distortions in diffusion-weighted EPI. *Neuroimage.* 2002; 16:177–199. [PubMed: 11969328]
- Augustinack JC, Helmer K, Huber KE, Kakunoori S, Zöllei L, Fischl B. Direct visualization of the perforant pathway in the human brain with ex vivo diffusion tensor imaging. *Front Hum Neurosci.* 2010; 4:42. [PubMed: 20577631]
- Bammer R. Basic principles of diffusion-weighted imaging. *Eur J Radiol.* 2003; 45:169–184. [PubMed: 12595101]
- Basser JP, Mattiello J, LeBihan D. Estimation of the effective self-diffusion tensor from the NMR spin echo. *J Magn Reson B.* 1994; 103:247–254. [PubMed: 8019776]
- Basser PJ, Pajevic S, Pierpaoli C, Duda J, Aldroubi A. In vivo fiber tractography using DT-MRI data. *Magn Reson Med.* 2000; 44:625–632. [PubMed: 11025519]

- Benes FM. Myelination of cortical-hippocampal relays during late adolescence. *Schizophr Bull.* 1989; 15:585–593. [PubMed: 2623440]
- Braak H, Braak E. Neuropathological staging of Alzheimer-related changes. *Acta Neuropathol.* 1991; 82:239–259. [PubMed: 1759558]
- Burggren AC, Zeineh MM, Ekstrom AD, Braskie MN, Thompson PM, Small GW, Bookheimer SY. Reduced cortical thickness in hippocampal subregions among cognitively normal apolipoprotein E e4 carriers. *Neuroimage.* 2008; 41:1177–1183. [PubMed: 18486492]
- Cook, P.; Bai, Y.; Nedjati-Gilani, S.; Seunarine, K.; Hall, M.; Parker, G.; Alexander, D. Camino: Open-source diffusion-MRI reconstruction and processing; 14th Scientific Meeting of the International Society for Magnetic Resonance in Medicine; 2006.
- Dauguet J, Peled S, Berezovskii V, Delzescaux T, Warfield SK, Born R, Westin C-F. Comparison of fiber tracts derived from in-vivo DTI tractography with 3D histological neural tract tracer reconstruction on a macaque brain. *Neuroimage.* 2007; 37:530–538. [PubMed: 17604650]
- Dice LR. Measures of the Amount of Ecologic Association Between Species. *Ecology.* 1945; 26:297–302.
- Dietrich O, Raya JG, Reeder SB, Reiser MF, Schoenberg SO. Measurement of signal-to-noise ratios in MR images: influence of multichannel coils, parallel imaging, and reconstruction filters. *J Magn Reson Imaging.* 2007; 26:375–385. [PubMed: 17622966]
- Duvernoy, HM. The human hippocampus: functional anatomy, vascularization, and serial sections with MRI. Berlin: Springer Verlag; 2005.
- Dyrby TB, Sogaard LV, Parker GJ, Alexander DC, Lind NM, Baaré WFC, Hay-Schmidt A, Eriksen N, Pakkenberg B, Paulson OB, Jelsing J. Validation of in vitro probabilistic tractography. *Neuroimage.* 2007; 37:1267–1277. [PubMed: 17706434]
- Embleton KV, Haroon HA, Morris DM, Ralph MAL, Parker GJM. Distortion correction for diffusion-weighted MRI tractography and fMRI in the temporal lobes. *Hum Brain Mapp.* 2010; 31:1570–1587. [PubMed: 20143387]
- Giannakopoulos P, Kövari E, Gold G, von Gunten A, Hof PR, Bouras C. Pathological substrates of cognitive decline in Alzheimer's disease. *Front Neurol Neurosci.* 2009; 24:20–29. [PubMed: 19182459]
- Goldman-Rakic PS, Selemon LD, Schwartz ML. Dual pathways connecting the dorsolateral prefrontal cortex with the hippocampal formation and parahippocampal cortex in the rhesus monkey. *Neuroscience.* 1984; 12:719–743. [PubMed: 6472617]
- Gómez-Isla T, Hollister R, West H, Mui S, Growdon JH, Petersen RC, Parisi JE, Hyman BT. Neuronal loss correlates with but exceeds neurofibrillary tangles in Alzheimer's disease. *Ann Neurol.* 1997; 41:17–24. [PubMed: 9005861]
- Gómez-Isla T, Price JL, McKeel DW Jr, Morris JC, Growdon JH, Hyman BT. Profound loss of layer II entorhinal cortex neurons occurs in very mild Alzheimer's disease. *J Neurosci.* 1996; 16:4491–4500. [PubMed: 8699259]
- Griswold MA, Jakob PM, Heidemann RM, Nittka M, Jellus V, Wang J, Kiefer B, Haase A. Generalized autocalibrating partially parallel acquisitions (GRAPPA). *Magn Reson Med.* 2002; 47:1202–1210. [PubMed: 12111967]
- Haselgrove JC, Moore JR. Correction for distortion of echo-planar images used to calculate the apparent diffusion coefficient. *Magn Reson Med.* 1996; 36:960–964. [PubMed: 8946363]
- Hevner RF, Kinney HC. Reciprocal entorhinal-hippocampal connections established by human fetal midgestation. *J Comp Neurol.* 1996; 372:384–394. [PubMed: 8873867]
- Holdsworth, S.; Skare, S.; Bammer, R. On the application of phase correction and use of k-space entropy in partial Fourier diffusion-weighted EPI; Proceedings 17th Scientific Meeting, International Society for Magnetic Resonance in Medicine; Honolulu. 2009. p. 4617
- Holdsworth SJ, Skare S, Newbould RD, Bammer R. Robust GRAPPA-accelerated diffusion-weighted readout-segmented (RS)-EPI. *Magn Reson Med.* 2009; 62:1629–1640. [PubMed: 19859974]
- Hyman BT, Van Hoesen GW, Damasio AR, Barnes CL. Alzheimer's disease: cell-specific pathology isolates the hippocampal formation. *Science.* 1984; 225:1168–1170. [PubMed: 6474172]
- Insausti, R.; Amaral, DG. The Human Nervous System. Second Edition. London: Academic Press; 2004. p. 871-914.

- Insausti R, Juottonen K, Soininen H, Insausti AM, Partanen K, Vainio P, Laakso MP, Pitkänen A. MR volumetric analysis of the human entorhinal, perirhinal, and temporopolar cortices. *AJNR Am J Neuroradiol*. 1998; 19:659–671. [PubMed: 9576651]
- Jenkinson M, Bannister P, Brady M, Smith S. Improved optimization for the robust and accurate linear registration and motion correction of brain images. *Neuroimage*. 2002; 17:825–841. [PubMed: 12377157]
- Jezzard P, Barnett AS, Pierpaoli C. Characterization of and correction for eddy current artifacts in echo planar diffusion imaging. *Magn Reson Med*. 1998; 39:801–812. [PubMed: 9581612]
- Jones DK. Determining and visualizing uncertainty in estimates of fiber orientation from diffusion tensor MRI. *Magn Reson Med*. 2003; 49:7–12. [PubMed: 12509814]
- Jones DK, Basser PJ. “Squashing peanuts and smashing pumpkins”: how noise distorts diffusion-weighted MR data. *Magn Reson Med*. 2004; 52:979–993. [PubMed: 15508154]
- Jones DK, Leemans A. Diffusion tensor imaging. *Methods Mol Biol*. 2011; 711:127–144. [PubMed: 21279600]
- Kalus P, Slotboom J, Gallinat J, Mahlberg R, Cattapan-Ludewig K, Wiest R, Nyffeler T, Buri C, Federspiel A, Kunz D, Schroth G, Kiefer C. Examining the gateway to the limbic system with diffusion tensor imaging: the perforant pathway in dementia. *Neuroimage*. 2006; 30:713–720. [PubMed: 16337815]
- Kerchner GA, Hess CP, Hammond-Rosenbluth KE, Xu D, Rabinovici GD, Kelley DAC, Vigneron DB, Nelson SJ, Miller BL. Hippocampal CA1 apical neuropil atrophy in mild Alzheimer disease visualized with 7-T MRI. *Neurology*. 2010; 75:1381–1387. [PubMed: 20938031]
- Köhler C. Morphological details of the projection from the presubiculum to the entorhinal area as shown with the novel PHA-L immunohistochemical tracing method in the rat. *Neurosci Lett*. 1984; 45:285–290. [PubMed: 6374516]
- Leemans A, Jones DK. The B-matrix must be rotated when correcting for subject motion in DTI data. *Magn Reson Med*. 2009; 61:1336–1349. [PubMed: 19319973]
- Lim C, Blume HW, Madsen JR, Saper CB. Connections of the hippocampal formation in humans: I. The mossy fiber pathway. *J Comp Neurol*. 1997; 385:325–351. [PubMed: 9300763]
- Lim C, Mufson EJ, Kordower JH, Blume HW, Madsen JR, Saper CB. Connections of the hippocampal formation in humans: II. The endfolial fiber pathway. *J Comp Neurol*. 1997; 385:352–371. [PubMed: 9300764]
- Malykhin N, Concha L, Seres P, Beaulieu C, Coupland NJ. Diffusion tensor imaging tractography and reliability analysis for limbic and paralimbic white matter tracts. *Psychiatry Res*. 2008; 164:132–142. [PubMed: 18945599]
- Mirra SS, Heyman A, McKeel D, Sumi SM, Crain BJ, Brownlee LM, Vogel FS, Hughes JP, van Belle G, Berg L. The Consortium to Establish a Registry for Alzheimer’s Disease (CERAD). Part II. Standardization of the neuropathologic assessment of Alzheimer’s disease. *Neurology*. 1991; 41:479–486. [PubMed: 2011243]
- Mufson EJ, Brady DR, Kordower JH. Tracing neuronal connections in postmortem human hippocampal complex with the carbocyanine dye DiI. *Neurobiol Aging*. 1990; 11:649–653. [PubMed: 1704107]
- Mufson EJ, Pandya DN. Some observations on the course and composition of the cingulum bundle in the rhesus monkey. *J Comp Neurol*. 1984; 225:31–43. [PubMed: 6725639]
- Müller MJ, Mazanek M, Weibrich C, Dellani PR, Stoeter P, Fellgiebel A. Distribution characteristics, reproducibility, and precision of region of interest-based hippocampal diffusion tensor imaging measures. *AJNR Am J Neuroradiol*. 2006; 27:440–446. [PubMed: 16484426]
- Nieuwenhuys, R.; Voogd, J.; Van Huijzen, C.; Van Huijzen, C. *The human central nervous system*. Springer Verlag; 2008.
- O’Mara S. The subiculum: what it does, what it might do, and what neuroanatomy has yet to tell us. *J Anat*. 2005; 207:271–282. [PubMed: 16185252]
- Ozarslan, E.; Koay, C.; Shepherd, T.; Blackband, S.; Basser, P. Simple harmonic oscillator based reconstruction and estimation for three-dimensional q-space MRI; Proceedings 17th Scientific Meeting, International Society for Magnetic Resonance in Medicine; Honolulu. 2009. p. 1396

- Parker GJM, Haroon HA, Wheeler-Kingshott CAM. A framework for a streamline-based probabilistic index of connectivity (PICO) using a structural interpretation of MRI diffusion measurements. *J Magn Reson Imaging*. 2003; 18:242–254. [PubMed: 12884338]
- Pipe JG, Farthing VG, Forbes KP. Multishot diffusion-weighted FSE using PROPELLER MRI. *Magn Reson Med*. 2002; 47:42–52. [PubMed: 11754441]
- Powell HWR, Guye M, Parker GJM, Symms MR, Boulby P, Koepp MJ, Barker GJ, Duncan JS. Noninvasive in vivo demonstration of the connections of the human parahippocampal gyrus. *Neuroimage*. 2004; 22:740–747. [PubMed: 15193602]
- Qu P, Shen GX, Wang C, Wu B, Yuan J. Tailored utilization of acquired k-space points for GRAPPA reconstruction. *J Magn Reson*. 2005; 174:60–67. [PubMed: 15809173]
- Reeder SB, Atalar E, Faranesh AZ, McVeigh ER. Referenceless interleaved echo-planar imaging. *Magn Reson Med*. 1999; 41:87–94. [PubMed: 10025615]
- Reese TG, Heid O, Weisskoff RM, Wedeen VJ. Reduction of eddy-current-induced distortion in diffusion MRI using a twice-refocused spin echo. *Magn Reson Med*. 2003; 49:177–182. [PubMed: 12509835]
- Rohde GK, Barnett AS, Basser PJ, Marengo S, Pierpaoli C. Comprehensive approach for correction of motion and distortion in diffusion-weighted MRI. *Magn Reson Med*. 2004; 51:103–114. [PubMed: 14705050]
- Rose SE, McMahon KL, Janke AL, O'Dowd B, de Zubicaray G, Strudwick MW, Chalk JB. Diffusion indices on magnetic resonance imaging and neuropsychological performance in amnesic mild cognitive impairment. *J Neurol Neurosurg Psychiatry*. 2006; 77:1122–1128. [PubMed: 16754694]
- Rosene DL, Van Hoesen GW. Hippocampal efferents reach widespread areas of cerebral cortex and amygdala in the rhesus monkey. *Science*. 1977; 198:315–317. [PubMed: 410102]
- Salmenpera TM, Simister RJ, Bartlett P, Symms MR, Boulby PA, Free SL, Barker GJ, Duncan JS. High-resolution diffusion tensor imaging of the hippocampus in temporal lobe epilepsy. *Epilepsy Res*. 2006; 71:102–106. [PubMed: 16870399]
- Shepherd TM, Ozarslan E, Yachnis AT, King MA, Blackband SJ. Diffusion tensor microscopy indicates the cytoarchitectural basis for diffusion anisotropy in the human hippocampus. *AJNR Am J Neuroradiol*. 2007; 28:958–964. [PubMed: 17494678]
- Skare, S.; Holdsworth, S.; Newbould, R.; Bammer, R. On the battle between Rician noise and phase-interferences in DWI; Proceedings 17th Scientific Meeting, International Society for Magnetic Resonance in Medicine; Honolulu. 2009. p. 1409
- Skare S, Newbould RD, Clayton DB, Albers GW, Nagle S, Bammer R. Clinical multishot DW-EPI through parallel imaging with considerations of susceptibility, motion, and noise. *Magn Reson Med*. 2007; 57:881–890. [PubMed: 17457876]
- Smith SM. Fast robust automated brain extraction. *Hum Brain Mapp*. 2002; 17:143–155. [PubMed: 12391568]
- Smith SM, Jenkinson M, Woolrich MW, Beckmann CF, Behrens TEJ, Johansen-Berg H, Bannister PR, De Luca M, Drobnjak I, Flitney DE, Niazy RK, Saunders J, Vickers J, Zhang Y, De Stefano N, Brady JM, Matthews PM. Advances in functional and structural MR image analysis and implementation as FSL. *Neuroimage*. 2004; 23(Suppl 1):S208–S219. [PubMed: 15501092]
- Suzuki WA, Amaral DG. Topographic organization of the reciprocal connections between the monkey entorhinal cortex and the perirhinal and parahippocampal cortices. *J Neurosci*. 1994; 14:1856–1877. [PubMed: 8126576]
- Swanson LW, Cowan WM. Hippocampo-hypothalamic connections: origin in subicular cortex, not ammon's horn. *Science*. 1975; 189:303–304. [PubMed: 49928]
- Swanson LW, Cowan WM. An autoradiographic study of the organization of the efferent connections of the hippocampal formation in the rat. *J Comp Neurol*. 1977; 172:49–84. [PubMed: 65364]
- Swanson LW, Wyss JM, Cowan WM. An autoradiographic study of the organization of intrahippocampal association pathways in the rat. *J Comp Neurol*. 1978; 181:681–715. [PubMed: 690280]
- Trojanowski JQ, Lee VMY. The role of tau in Alzheimer's disease. *Med Clin North Am*. 2002; 86:615–627. [PubMed: 12168561]

- Van Hoesen GW, Hyman BT, Damasio AR. Entorhinal cortex pathology in Alzheimer's disease. *Hippocampus*. 1991; 1:1–8. [PubMed: 1669339]
- Van Hoesen GW, Pandya DN. Some connections of the entorhinal (area 28) and perirhinal (area 35) cortices of the rhesus monkey. III. Efferent connections. *Brain Res*. 1975; 95:39–59. [PubMed: 1156868]
- Van Leemput K, Bakkour A, Benner T, Wiggins G, Wald LL, Augustinack J, Dickerson BC, Golland P, Fischl B. Automated segmentation of hippocampal subfields from ultra-high resolution in vivo MRI. *Hippocampus*. 2009; 19:549–557. [PubMed: 19405131]
- Witter MP, Van Hoesen GW, Amaral DG. Topographical organization of the entorhinal projection to the dentate gyrus of the monkey. *J Neurosci*. 1989; 9:216–228. [PubMed: 2913203]
- Woolrich MW, Jbabdi S, Patenaude B, Chappell M, Makni S, Behrens T, Beckmann C, Jenkinson M, Smith SM. Bayesian analysis of neuroimaging data in FSL. *Neuroimage*. 2009; 45:S173–S186. [PubMed: 19059349]
- Xu, D. Correcting High Order Eddy Current Induced Distortion for Diffusion Weighted Echo Planar Imaging; Proceedings 19th Scientific Meeting, International Society for Magnetic Resonance in Medicine; Montreal. 2011. p. 4564
- Yassa MA, Muftuler LT, Stark CEL. Ultrahigh-resolution microstructural diffusion tensor imaging reveals perforant path degradation in aged humans in vivo. *Proc Natl Acad Sci U S A*. 2010; 107:12687–12691. [PubMed: 20616040]
- Yushkevich PA, Avants BB, Pluta J, Das S, Minkoff D, Mechanic-Hamilton D, Glynn S, Pickup S, Liu W, Gee JC, Grossman M, Detre JA. A high-resolution computational atlas of the human hippocampus from postmortem magnetic resonance imaging at 9.4 T. *Neuroimage*. 2009; 44:385–398. [PubMed: 18840532]
- Yushkevich PA, Piven J, Hazlett HC, Smith RG, Ho S, Gee JC, Gerig G. User-guided 3D active contour segmentation of anatomical structures: significantly improved efficiency and reliability. *Neuroimage*. 2006; 31:1116–1128. [PubMed: 16545965]
- Yushkevich PA, Wang H, Pluta J, Das SR, Craige C, Avants BB, Weiner MW, Mueller S. Nearly automatic segmentation of hippocampal subfields in in vivo focal T2-weighted MRI. *Neuroimage*. 2010; 53:1208–1224. [PubMed: 20600984]
- Zeineh MM, Engel SA, Thompson PM, Bookheimer SY. Dynamics of the hippocampus during encoding and retrieval of face-name pairs. *Science*. 2003; 299:577–580. [PubMed: 12543980]
- Zeineh MM, Holdsworth S, Skare S, Atlas SW, Bammer R. Challenges of High-resolution Diffusion Imaging of the Human Medial Temporal Lobe in Alzheimer Disease. *Top Magn Reson Imaging*. 2010; 21:355–365. [PubMed: 22158129]

Highlights

Once-refocused axial plane parallel acquisition optimizes SNR & minimizes Distortion

Higher-order eddy-current correction and motion compensation improve image Fidelity

High-resolution imaging facilitates tractography of the entire MTL

MTL FA, MD, and fiber parameters show a L-R asymmetry correlating with language dominance

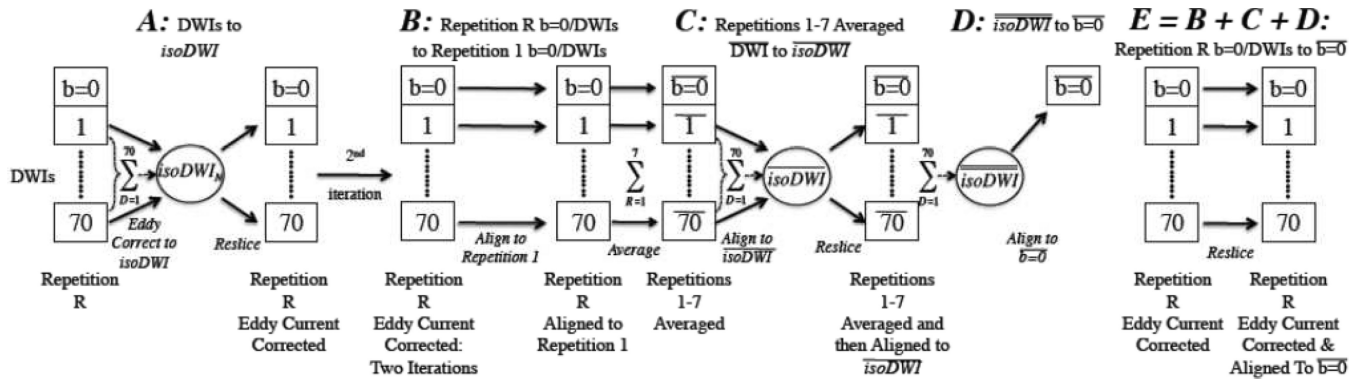


Figure 1. Diffusion-weighted imaging pre-processing pipeline. See 2.1.2.

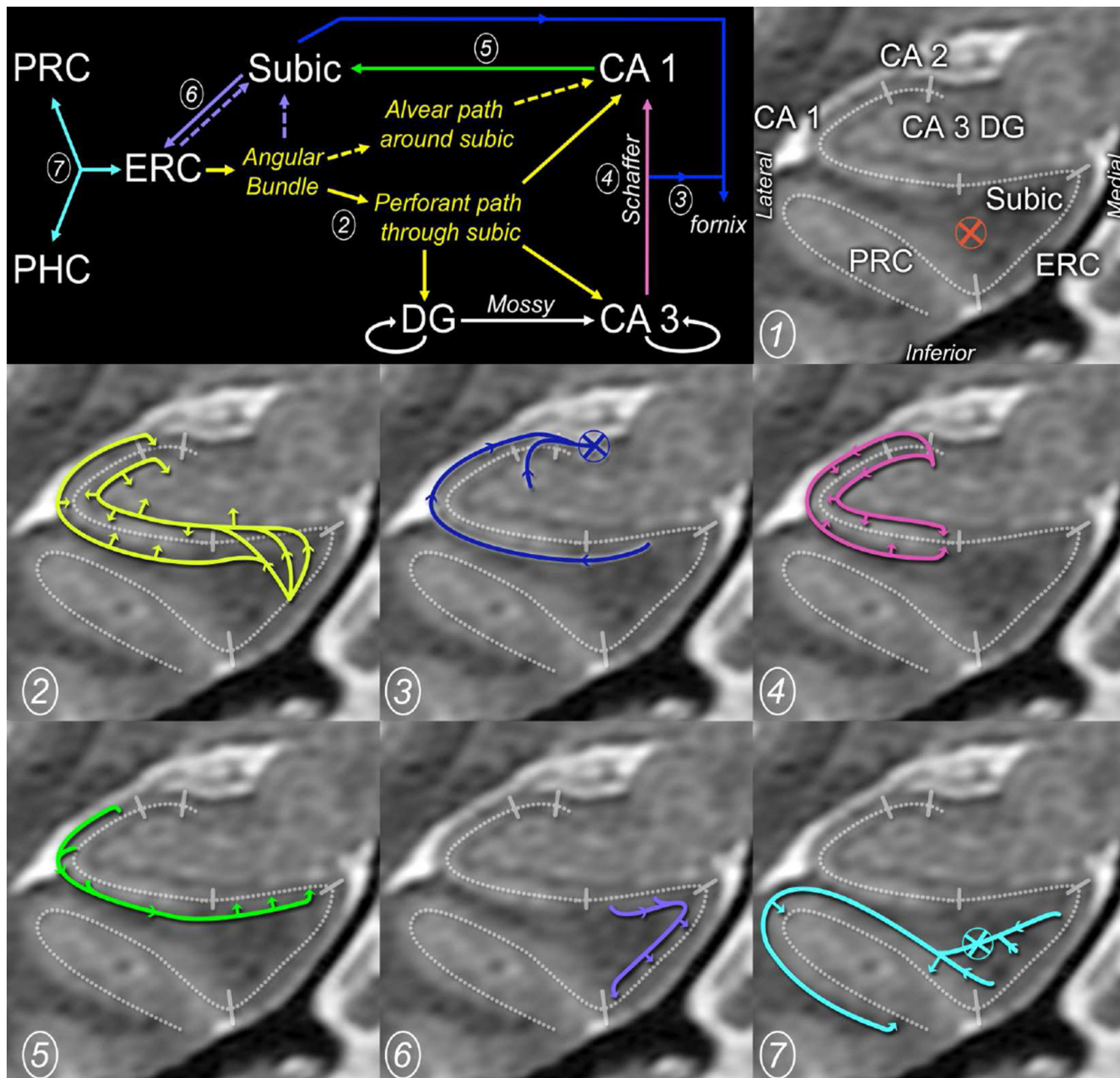


Figure 2. Medial temporal lobe neuroanatomy. At the top left is a color-coded diagram of medial temporal circuitry. Subregions are labeled on the overlaid coronal MR at the top right. Crosshairs denote tracks that run through plane. Pathways of interest: (1) parahippocampal cingulum bundle, which runs almost exclusively through-plane, (2) perforant (internal) and alvear (external) pathways, (3) CA3 and subicular projections to the fornix, (4) Schaffer collaterals from CA 3 to CA 1, (5) CA 1 to subiculum, (6) subiculum to entorhinal cortex, (7) entorhinal to perirhinal/parahippocampal cortex.

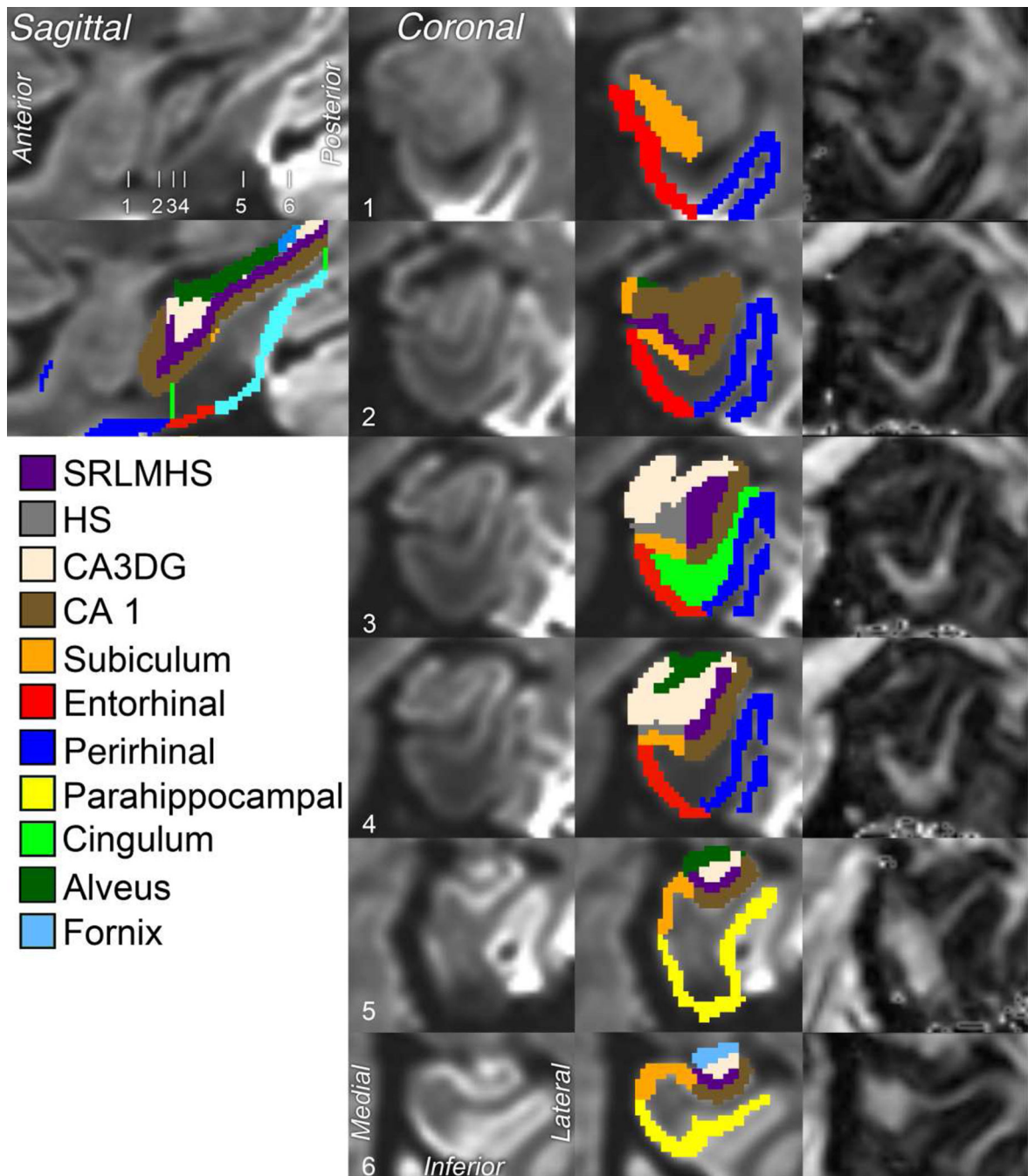


Figure 3. Segmentation Procedure: Coronal slabs 1–6 progress anteriorly to posteriorly on this left hemisphere. Slabs 1–4 constitute the hippocampal head, slab 5 represents the hippocampal body, and slab 6 represents the posterior-most hippocampal body. All images are isoDWI except for the far right column, which is a co-planar fractional anisotropy map.

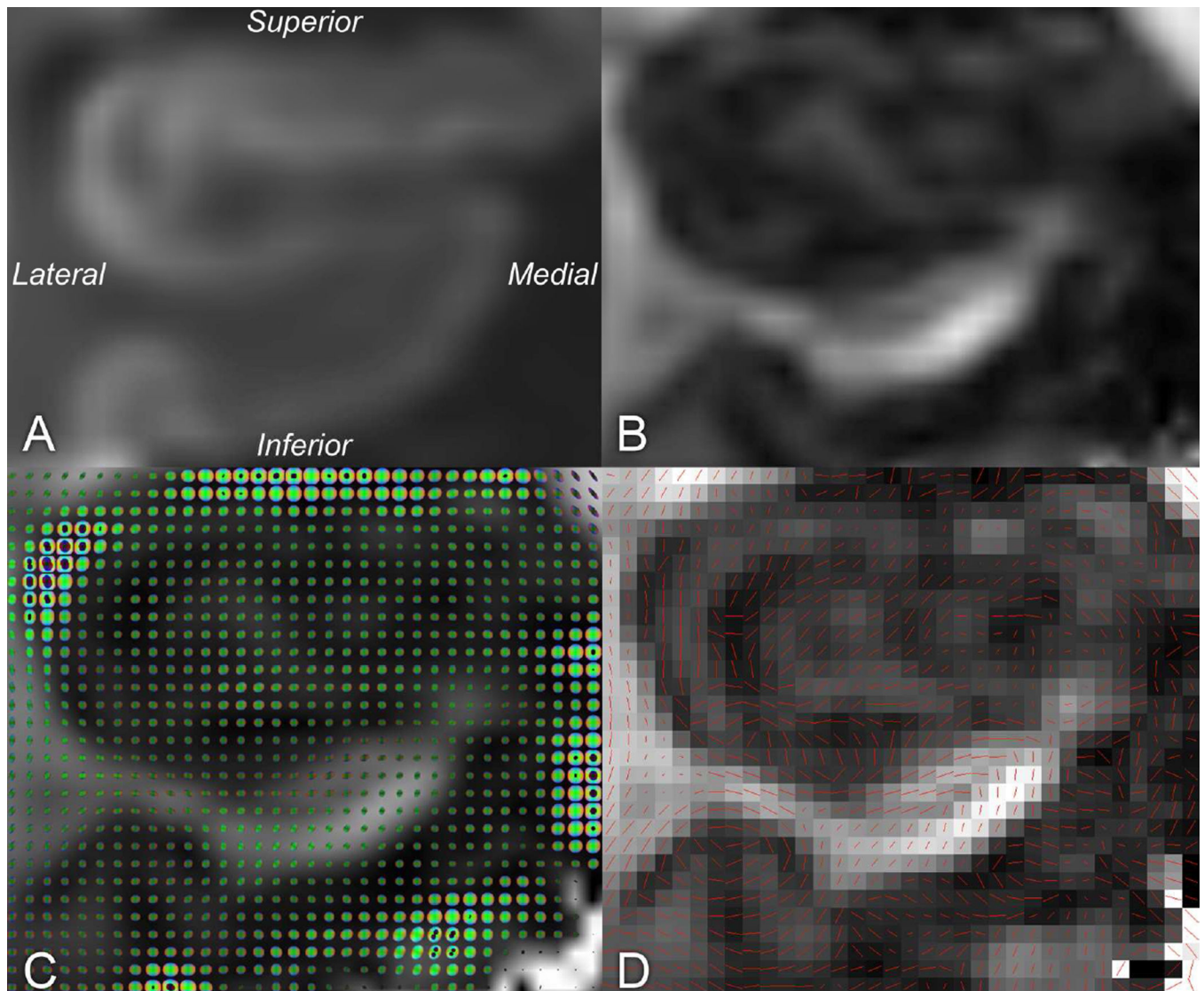


Figure 4. Example high-resolution images of the right hippocampus from one subject. A) coronal isoDWI. B) coronal fractional anisotropy map. C) diffusion tensor ellipsoids. D) direction of principle eigenvector.

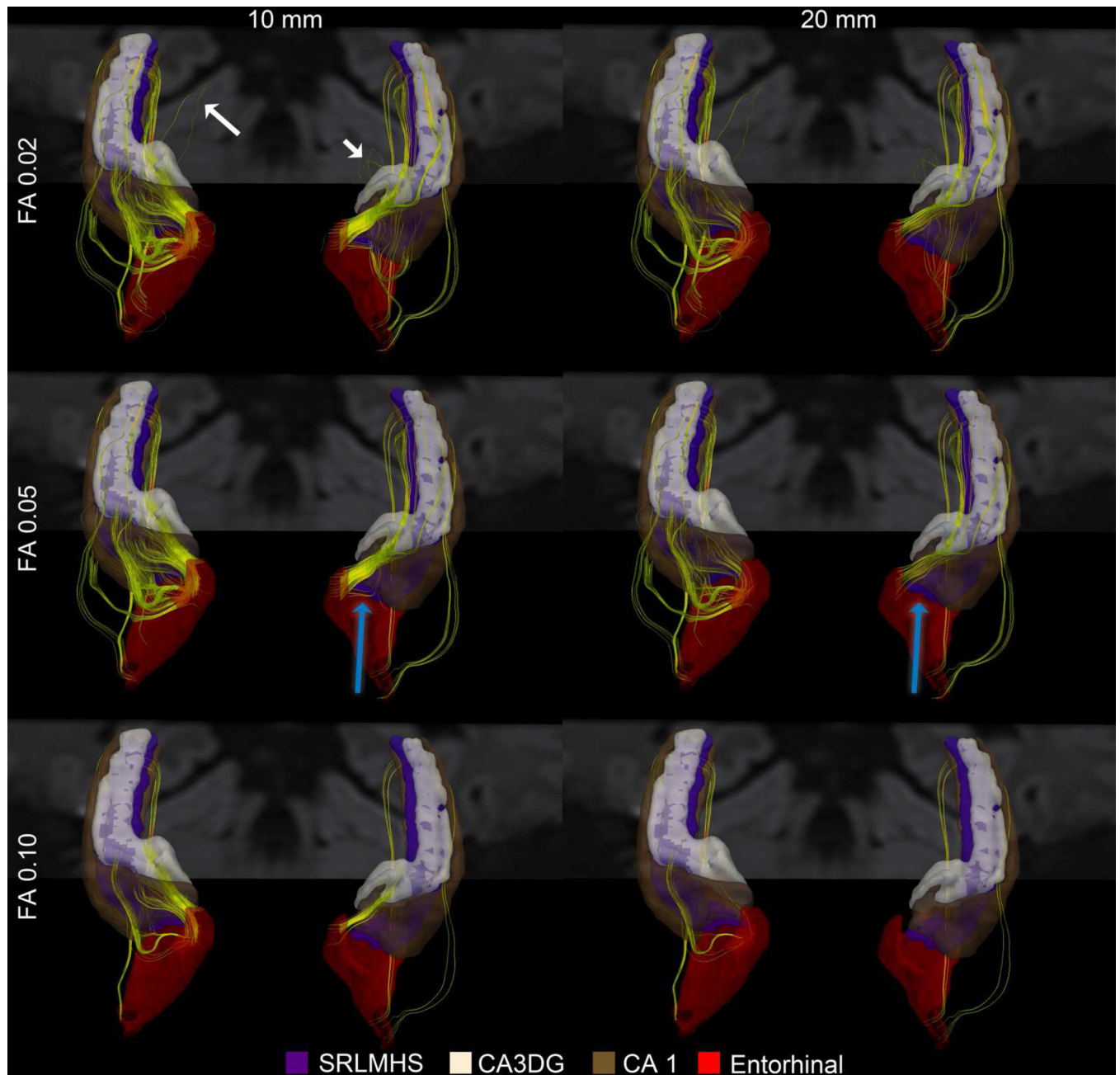
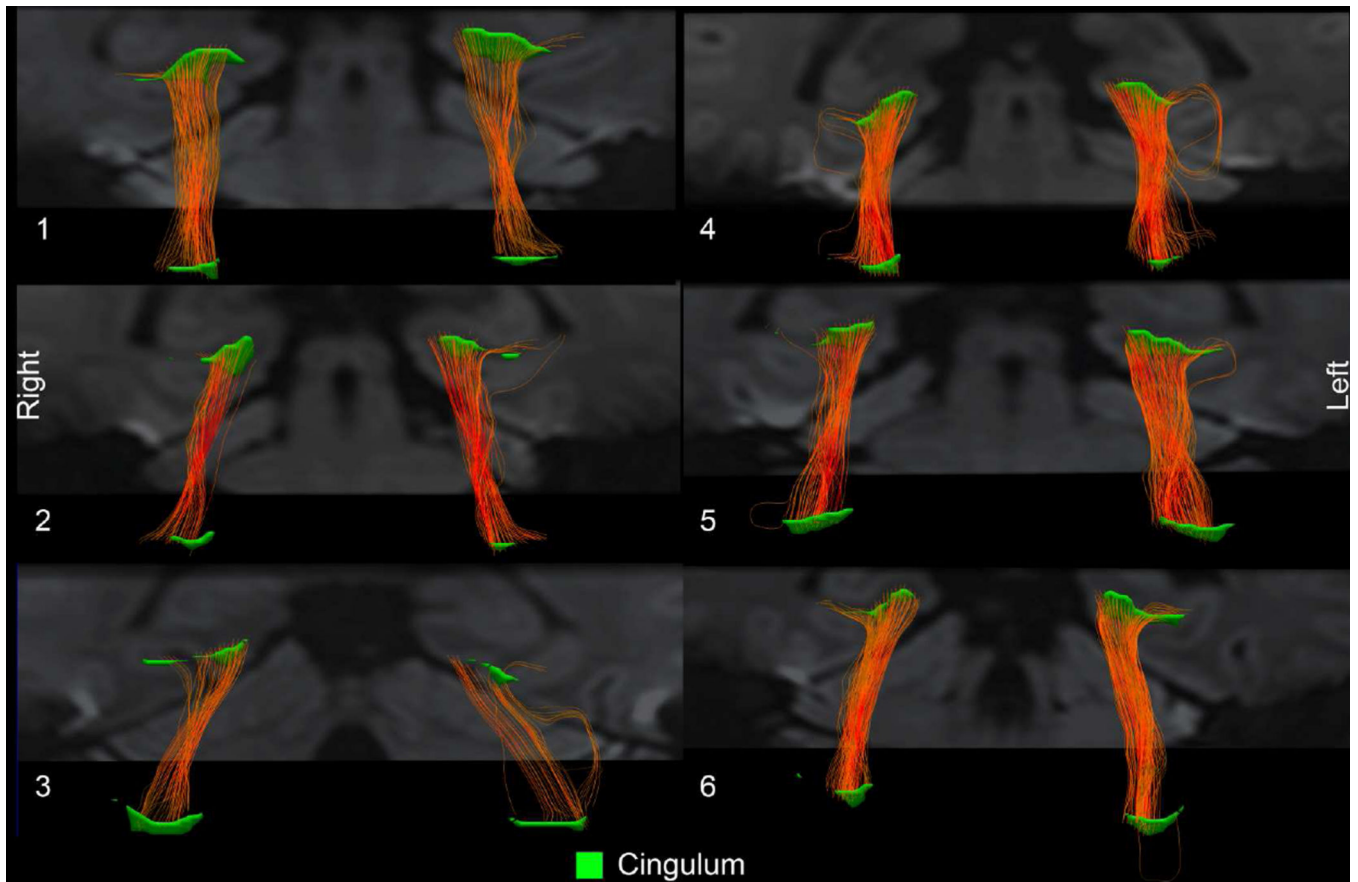
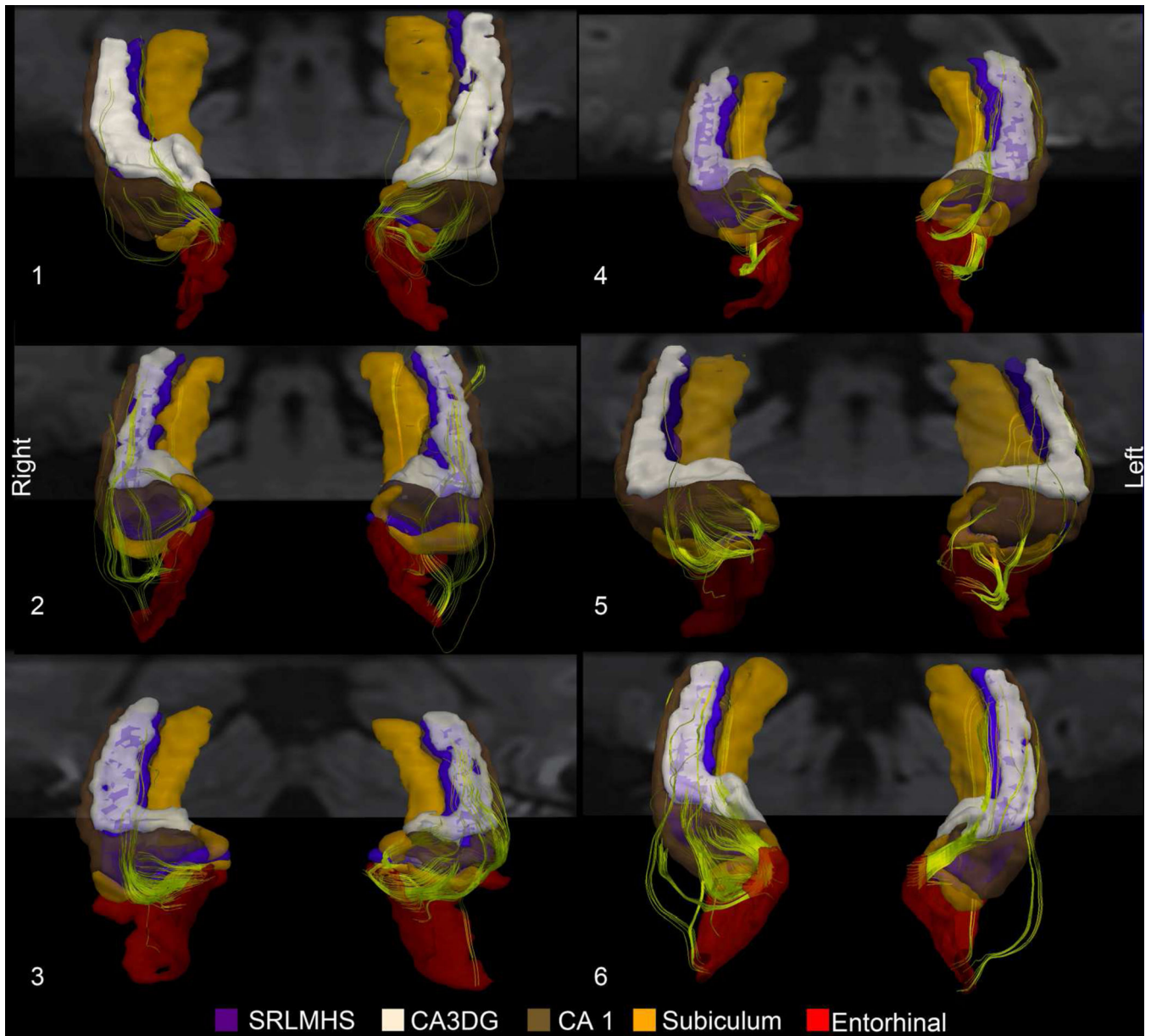


Figure 5. Tractography Parameter Optimization. In one subject, tracts are depicted with anisotropy thresholds of 0.02, 0.05, and 0.1 as well as minimum tract lengths of 10 and 20 mm, all utilizing a curvature threshold of 40 degrees. White arrows correspond to false positives transgressing CSF. Blue arrows correspond to a track seen only on the shorter minimum tract length threshold.



6-1

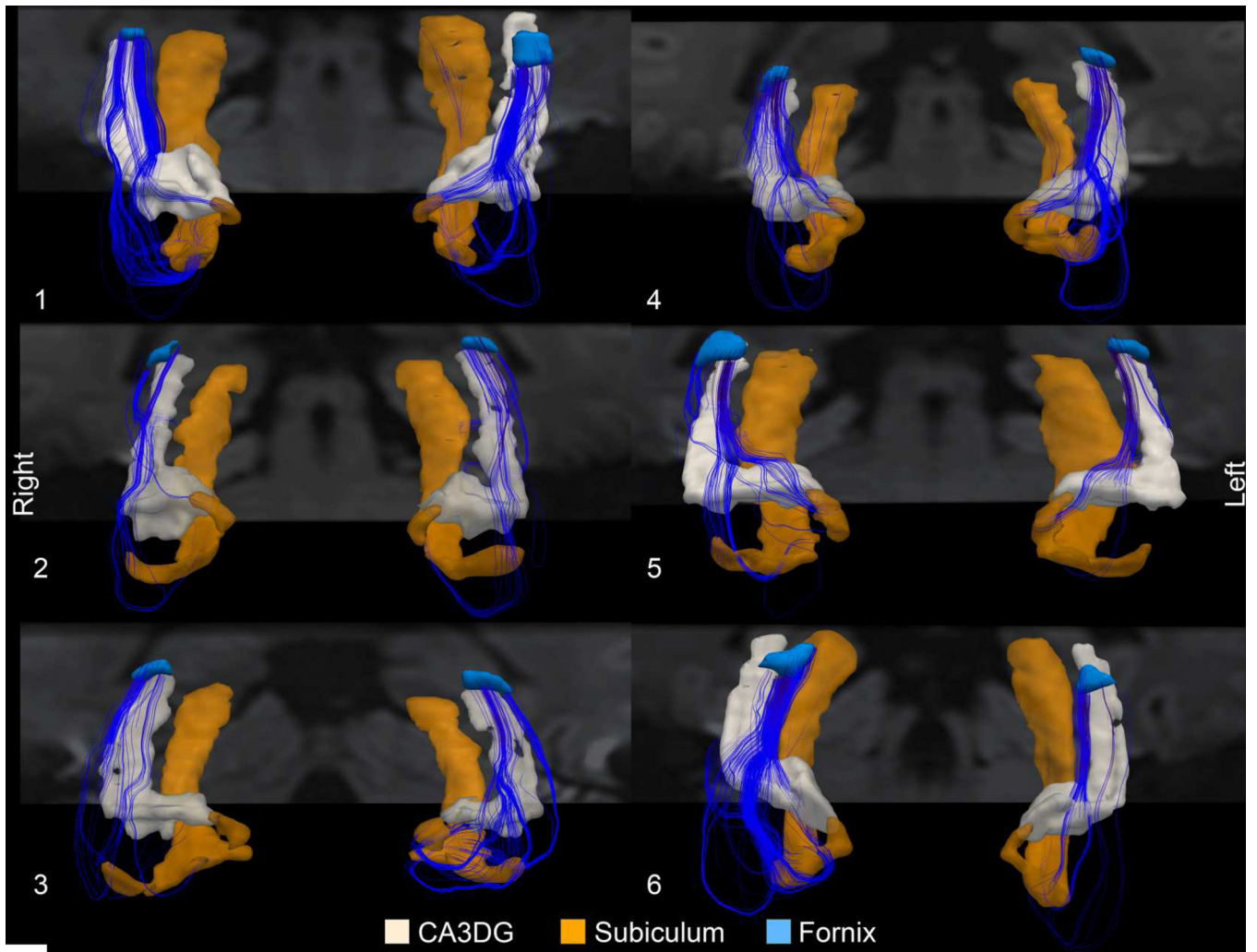
Figure 6-1. Parahippocampal cingulum bidirectional tractography in all 6 subjects. The color scale for the fiber pathways and subregions corresponds to that used in Figures 2 and 3, respectively.



6-2

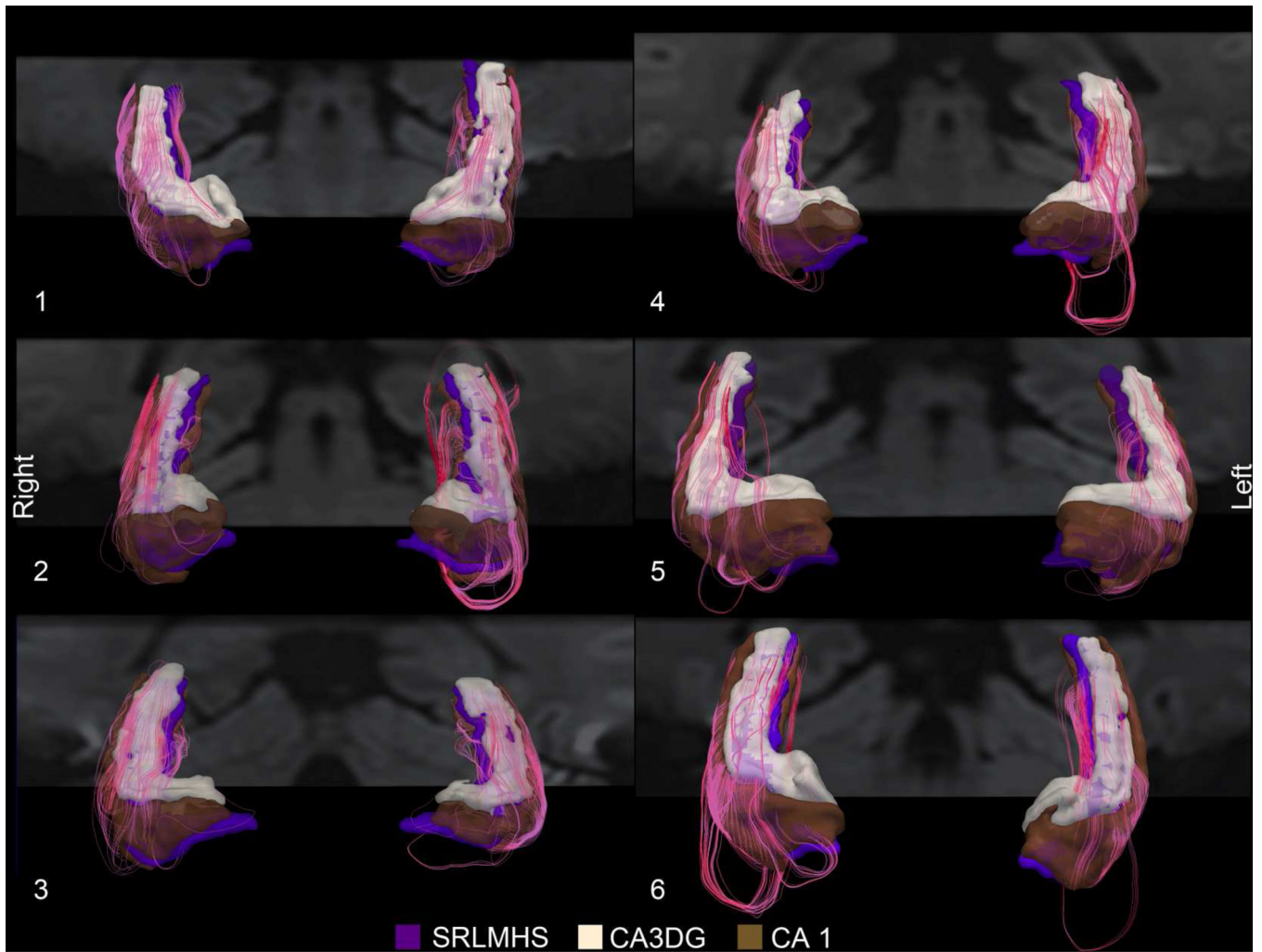
Figure 6-2.

Perforant pathway between the entorhinal cortex and CA3DG, CA 1, and SRLMHS. Perforant pathway fibers should project through the subiculum (which is also shown but is neither a seed nor a target for this pathway), while the alvear path fibers should extend around the hippocampus.



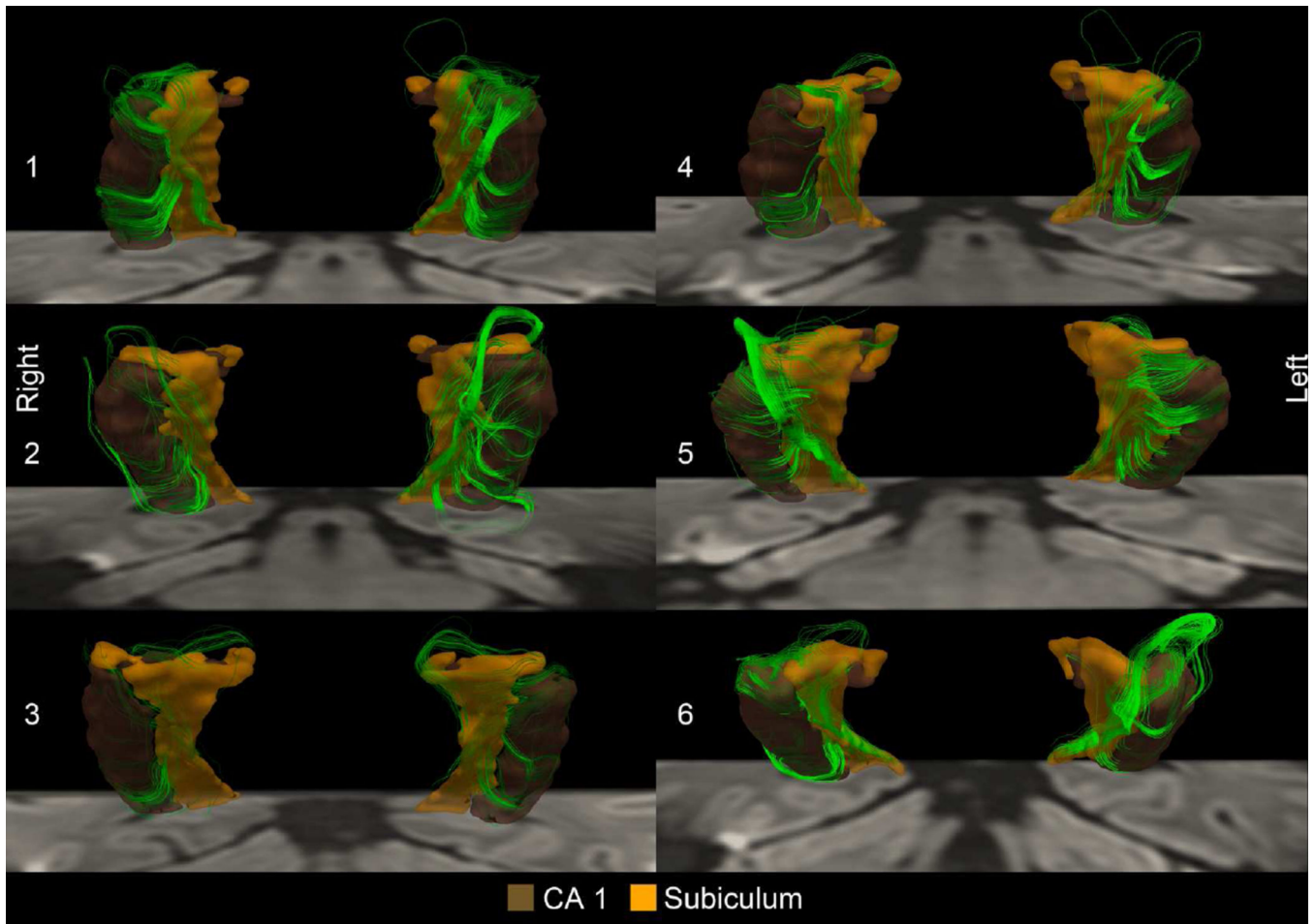
6-3

Figure 6-3.
CA3 and subicular projections to the fornix.



6-4

Figure 6-4.
Schaffer collaterals from CA 3 to CA 1/SRLMHS



6-5

Figure 6-5.
CA 1 to subiculum

Table 1

Subregion Analysis: median fractional anisotropy and median mean diffusivity, averaged across subjects (Mean \pm SD). ¹ Paired t-test $p < 0.05$, uncorrected (n=6).

	FA (L / R)	MD (mm ² /s)
<i>ERC</i>	0.158 \pm 0.009 / 0.144 \pm 0.012 ¹	647 \pm 38 / 659 \pm 30
<i>PRC</i>	0.149 \pm 0.014 / 0.147 \pm 0.006	659 \pm 46 / 670 \pm 27
<i>PHC</i>	0.167 \pm 0.015 / 0.165 \pm 0.009	661 \pm 16 / 665 \pm 14
<i>CAISRLMHS</i>	0.132 \pm 0.007 / 0.129 \pm 0.009	704 \pm 26 / 706 \pm 29
<i>CA23DG</i>	0.148 \pm 0.012 / 0.149 \pm 0.013	722 \pm 26 / 724 \pm 38
<i>Subic</i>	0.185 \pm 0.010 / 0.190 \pm 0.013	655 \pm 22 / 662 \pm 35
<i>Alveus & Fornix</i>	0.230 \pm 0.024 / 0.214 \pm 0.030	828 \pm 79 / 886 \pm 87 ¹

Table 2

Identification of Tractography Parameters: Mean number of bilateral ERC to CA123DGSRMHS bidirectional tracks (seven acquisition subset / one acquisition subset) under different curvature, minimum tract length, and FA thresholds, averaged across all subjects. This illustrates that parameter choices can influence sensitivity to presumed real tracks as well as sensitivity to noise.

	<i>Minimum Tract Length Threshold (mm.)</i>					
	10			20		
	<i>FA 0.02</i>	<i>FA 0.05</i>	<i>FA 0.10</i>	<i>FA 0.02</i>	<i>FA 0.05</i>	<i>FA 0.10</i>
20	50/9	49/9	33/8	5/3	5/3	3/3
30	172/65	162/65	70/49	44/19	42/19	8/14
40	356/182	303/180	98/114	143/61	114/61	14/35
50	572/354	443/346	117/181	281/141	199/137	21/59
60	824/557	577/530	134/236	450/259	280/238	28/82
70	1121/783	706/727	143/278	673/416	365/368	31/102
80	1406/1030	824/931	151/318	895/603	445/514	35/122
90	1686/1294	926/1149	157/356	1140/824	526/695	38/145

Curvature Threshold (degrees)

Table 3

Tractography: Fiber counting across medial temporal pathways. 1) Mean \pm standard deviation of the number of fibers across subjects, 2) Range (minimum and maximum) of the number of fibers, and 3) Mean \pm standard deviation of the ratio of the number of left-sided to the number of right-sided fibers.

	Mean \pm St. Dev (L / R)	Min - Max (L / R)	L:R Ratio
<i>Cingulum</i>	88 \pm 36 / 77 \pm 28	39 – 123 / 42 – 115	1.18 \pm 0.42
<i>Perforant</i>	144 \pm 106 / 159 \pm 111	42 – 349 / 72 – 377	1.17 \pm 0.91
<i>Fornix</i>	107 \pm 58 / 183 \pm 173	54 – 204 / 64 – 509	0.92 \pm 0.62
<i>Schafer</i>	289 \pm 52 / 280 \pm 124	216 – 368 / 188 – 484	1.15 \pm 0.37
<i>CA1 - Subiculum</i>	357 \pm 109 / 342 \pm 213	206 – 506 / 157 – 660	1.27 \pm 0.53
<i>Subiculum - ERC</i>	309 \pm 155 / 250 \pm 249	129 – 523 / 72 – 747	2.01 \pm 1.88
<i>ERC - PRC/PHC</i>	425 \pm 173 / 349 \pm 111	222 – 656 / 201 – 480	1.21 \pm 0.24

Table 4

Tractography: Fractional anisotropy and mean diffusivity measured across fiber tracks (Mean \pm SD). No statistically significant differences were identified when comparing individual tracks between hemispheres.

	<i>Fractional Anisotropy (L / R)</i>	<i>Mean Diffusivity (L / R)</i>	<i>Length (L / R)</i>
<i>Cingulum</i>	0.483 \pm 0.031 / 0.493 \pm 0.027	642 \pm 34 / 646 \pm 43	31 \pm 3 / 29 \pm 2
<i>Perforant</i>	0.231 \pm 0.029 / 0.203 \pm 0.018	754 \pm 87 / 735 \pm 28	29 \pm 14 / 19 \pm 3
<i>Fornix</i>	0.307 \pm 0.039 / 0.265 \pm 0.029	810 \pm 16 / 843 \pm 52	33 \pm 8 / 28 \pm 2
<i>Schafer</i>	0.191 \pm 0.019 / 0.189 \pm 0.024	780 \pm 31 / 811 \pm 45	19 \pm 6 / 17 \pm 3
<i>CAI - Subiculum</i>	0.226 \pm 0.041 / 0.210 \pm 0.023	742 \pm 51 / 767 \pm 35	21 \pm 8 / 19 \pm 5
<i>Subiculum - ERC</i>	0.317 \pm 0.040 / 0.311 \pm 0.029	669 \pm 53 / 687 \pm 53	24 \pm 5 / 24 \pm 4
<i>ERC - PRC/PHC</i>	0.306 \pm 0.031 / 0.306 \pm 0.069	642 \pm 47 / 654 \pm 48	19 \pm 2 / 20 \pm 3

Table 5

Fiber counts from tractography of acquisition subsets (L/R).

	Cingulum	Perforant	Fornix	Schaefer	CA1 Subiculum	Subiculum ERC	ERC PRC/PHC	L:R Ratio P-value
7	88 ± 36 / 77 ± 28	144 ± 106 / 159 ± 111	107 ± 58 / 183 ± 173	289 ± 52 / 280 ± 124	357 ± 109 / 342 ± 213	309 ± 155 / 250 ± 249	425 ± 173 / 349 ± 111	0.050
First 6	88 ± 32 / 80 ± 30	163 ± 96 / 167 ± 113	97 ± 73 / 183 ± 167	257 ± 57 / 274 ± 119	328 ± 80 / 320 ± 206	314 ± 158 / 235 ± 205	405 ± 178 / 345 ± 109	0.055
5	88 ± 33 / 78 ± 29	148 ± 82 / 188 ± 156	85 ± 54 / 188 ± 163	265 ± 75 / 274 ± 101	325 ± 100 / 303 ± 167	267 ± 140 / 223 ± 187	363 ± 160 / 368 ± 111	0.273
4	83 ± 33 / 77 ± 25	143 ± 88 / 184 ± 206	85 ± 65 / 168 ± 160	250 ± 67 / 272 ± 109	273 ± 85 / 284 ± 156	269 ± 168 / 200 ± 174	351 ± 141 / 370 ± 124	0.190
Subsets								
First 3	81 ± 29 / 73 ± 29	118 ± 99 / 199 ± 177	82 ± 64 / 168 ± 143	226 ± 71 / 245 ± 95	250 ± 88 / 287 ± 157	265 ± 158 / 183 ± 176	317 ± 156 / 334 ± 113	0.334
Last 3	80 ± 29 / 69 ± 21	103 ± 54 / 117 ± 88	75 ± 35 / 144 ± 145	221 ± 54 / 241 ± 82	287 ± 89 / 294 ± 159	224 ± 112 / 242 ± 223	362 ± 217 / 292 ± 137	0.189
2	74 ± 23 / 67 ± 30	157 ± 106 / 142 ± 52	92 ± 46 / 156 ± 142	177 ± 23 / 226 ± 92	219 ± 108 / 254 ± 127	212 ± 144 / 202 ± 137	283 ± 122 / 292 ± 129	0.579
1	55 ± 25 / 52 ± 21	93 ± 51 / 88 ± 101	56 ± 25 / 118 ± 156	137 ± 58 / 149 ± 75	156 ± 86 / 179 ± 100	189 ± 135 / 158 ± 110	218 ± 105 / 189 ± 90	0.055

Dice coefficients from tractography of acquisition subsets (L/R), comparing the noted subset with the full 7-repetition dataset. The last row compares the first 3 to the last 3 repetitions.

Table 6

	Cingulum	Perforant	Fornix	Schafer	CA1 – Subiculum	Subiculum – ERC	ERC – PRC/PHC
First 6	0.90 ± 0.04	0.64 ± 0.07	0.70 ± 0.06	0.73 ± 0.03	0.72 ± 0.06	0.79 ± 0.05	0.78 ± 0.06
5	0.87 ± 0.03	0.58 ± 0.05	0.64 ± 0.07	0.68 ± 0.03	0.67 ± 0.06	0.72 ± 0.07	0.73 ± 0.06
4	0.84 ± 0.05	0.53 ± 0.05	0.57 ± 0.08	0.63 ± 0.04	0.60 ± 0.08	0.66 ± 0.10	0.69 ± 0.06
First 3	0.81 ± 0.05	0.48 ± 0.06	0.52 ± 0.07	0.57 ± 0.03	0.56 ± 0.08	0.62 ± 0.10	0.64 ± 0.07
Last 3	0.82 ± 0.05	0.44 ± 0.08	0.50 ± 0.09	0.58 ± 0.06	0.56 ± 0.07	0.64 ± 0.09	0.65 ± 0.07
2	0.79 ± 0.06	0.42 ± 0.07	0.48 ± 0.05	0.51 ± 0.05	0.50 ± 0.08	0.58 ± 0.10	0.60 ± 0.10
1	0.70 ± 0.08	0.27 ± 0.07	0.36 ± 0.06	0.41 ± 0.03	0.38 ± 0.11	0.49 ± 0.10	0.50 ± 0.09
First 3/ Last 3	0.75 ± 0.06	0.33 ± 0.08	0.39 ± 0.12	0.46 ± 0.05	0.44 ± 0.09	0.52 ± 0.09	0.54 ± 0.09